Geologia USP Série Científica

https://doi.org/10.11606/issn.2316-9095.v24-194388
Revista do Instituto de Geociências - USP
Geol. USP, Sér. cient., São Paulo, v. 24, n. 4, p. 39-62, 2024

Metallogenic characterization of the Aguinaldo structurally-controlled Epithermal gold occurrence, Alta Floresta Gold Province (Brazil)

Contexto metalogenético do garimpo filonar de Au ± Cu do Aguinaldo, Província Aurífera de Alta Floresta (MT)

Rômulo Bortolozzo[1], Rafael Rodrigues de Assis[2], Lorenzzo Cassaro[3], Lays Helmer Mengal[3]

[1] Universidade Estadual Paulista “Júlio de Mesquita Filho”, Instituto de Geociências e Ciências Exatas. Av. 24 A, 1515, Bela Vista, CEP 13506-692, Rio Claro, SP, Brazil. (romulo.bortolozzo@hotmail.com)
[2] Universidade de São Paulo, Instituto de Geociências. São Paulo, SP, Brazil. (assis.rafael@usp.br)
[3] Universidade de São Paulo, Instituto de Geociências, Programa de Pós-Graduação em Recursos Minerais e Hidrogeologia. São Paulo, SP, Brazil. (lcassaro95@usp.br; lays.mengal@usp.br)

Received on January 25, 2022; accepted on November 5, 2024.

ABSTRACT

In the eastern-southeast sector of Alta Floresta Gold Province (Amazon Craton), the 1.78 – 1.77 Ga calc-alkaline magmatism is interpreted as answerable for ore-forming processes responsible for its disseminated, vein-type, and filonar gold occurrences hosted in 2.05 – 1.77 Ga units. The Aguinaldo structurally-controlled gold occurrence exhibits ore zones hosted in 0.5 – 1.5m thick quartz + sulfide ± carbonate veins crosscutting the porphyroblastic mylonite orthogneiss, with SHRIMP U-Pb-zircon concordia crystallization age of 1,984.9 ± 5.2 Ma. Distal to ore zones are observed high temperature, intensive, and pervasive (1) albite-rich alteration, followed by (2) K-Feldspar alteration, telescoped by lower temperature pervasive alterations: (3) sericite-muscovite alteration, (4) silicification and silica infills; (5) carbonate alteration, (6) chlorite alteration, and (7) late veinlet-type quartz. The silica injection represents one of the major hydrothermal stages due to generating barren quartz veins and quartz ± carbonate vein with chalcopyrite + pyrite ± gold ± silver ± sphalerite ± galena ± bismuthinite veins. Although the veins are partially deformed, local comb-quartz texture remains preserved. Gold occurs as small inclusions or in contact with pyrite and chalcopyrite, and subordinately, in sphalerite. Electron microprobe analysis indicates chlorite of brunsvigite composition formed between 242° and 420° C, whereas white mica shows low phengite contents. The polymetallic veins signature, the high chalcopyrite contents with galena and sphalerite inclusions, the comb-texture quartz veins, together with the hydrothermal alteration sequence, suggest low to moderate temperature, neutral to slightly alkaline pH, and moderate fO_2 and fS_2 conditions, possibly triggered by boiling process. This scenario indicates intermediate-sulfidation epithermal ore-forming processes as the responsible for the genesis of Aguinaldo gold occurrence.

Keywords: Granitogenesis; Rondônia state, magma mingling; San Ignacio orogeny; Meso-proterozoic; Granitic magma sources; LA–ICP–MS.

RESUMO

No setor leste-sudeste da Província Aurífera de Alta Floresta (Cráton Amazônico), o magmatismo cálcio-alcalino de ca. 1,78 – 1,77 Ga, é interpretado como responsável pela geração de suas ocorrências auríferas disseminadas, venulares e filonares hospedadas em unidades de 2,05 – 1,77 Ga. A ocorrência aurífera estruturalmente controlada do Aguinaldo, está alojada em veios de quartzo + sulfetos ± carbonato de 0,5 – 1,5 m que truncam milonito de ortognaisse porfiroblástico, com idade de cristalização U-Pb em zircão (SHRIMP) de 1,984.9 ± 5.2 Ma. Os setores marginais ao minério são representados por alterações hidrotermais de alta temperatura e estilo pervasivo, que incluem: (1) geração de albita, seguida pela (2) formação de K-Feldspato, ambas telescopadas por alterações hidrotermais de menor temperatura. Esses estágios são representados por: (3) alteração com sericita-muscovita, (4) silicificação e injeção de sílica; (5) alteração carbonática, (6) alteração clorítica, e (7) vênulas tardias de quartzo. A injeção de sílica é um dos mais importantes estágios hidrotermais, pois permitiu a geração de veios estéreis de quartzo, e veios de quartzo ± carbonato, com calcopirita + pirita ± ouro ± prata ± esfalerita ± galena ± bismutinita. Embora parcialmente deformados, setores com quartzo em textura tipo-pente permanecem preservados. Ouro ocorre tanto como pequenas inclusões como em contato com calcopirita e pirita, e subordinadamente com esfalerita. Análises em microssonda indicam clorita essencialmente do tipo brunsvigita, gerada entre 242 e 420° C, enquanto a mica branca exibe baixo conteúdo fengítico. A assinatura polimetálica dos veios, os altos volumes de calcopirita com inclusões de galena e esfalerita, a textura em pente preservada, em conjunto à evolução paragenética da alteração hidrotermal, sugere condições de baixa a moderada temperatura, pH neutro a levemente alcalino, e moderado estado redox, possivelmente derivado de mecanismos de ebulição. Esse cenário indica a atuação de processos mineralizantes similares aos observados em depósitos epitermais intermediate-sulfidation, como responsáveis pela geração da ocorrência aurífera do Aguinaldo.

Palavras-chave: Granitogênese; Estado de Rondônia, mistura de magma; Orogenia San Ignacio; Mesoproterozoico; Fontes de magmas; LA-ICP-MS.

INTRODUCTION

The Amazon Craton (AC) configures an extensive Arquean platform, partially reworked and reactivated throughout the Proterozoic and stabilized at ca. 1.0 Ga (Amaral, 1974; Almeida, 1978; Tassinari and Macambira, 1999). The craton was the scenario of multiples orogenetic events that resulted in a variety of granitic, plutonic, volcanics, and volcaniclastic units derived from wide Paleoproterozoic calc-alkaline oxidized magmatism (Dall'Agnol et al., 2005; Juliani et al., 2005; Juliani and Fernandes, 2010; Alves et al., 2019). During the last decades, the magmatic events that took place in the AC have attracted attention of mining companies and researchers, with consequent identification of several gold-silver and base-metal occurrences, besides world-class base-metal, rare, and precious deposits (Juliani et al., 2005, 2014; Bettencourt et al., 2016; Assis et al., 2017).

Within this conjecture emerges the Alta Floresta Gold Province (AFGP) (Dardenne and Schobbenhaus, 2001), in the tectonic Juruena-Teles Province (Souza et al., 2005; Silva and Abram, 2008; Alves et al., 2019). Between the 1980 and 1990 decades, the Province has achieved prominence in the mineral national panorama due to its considerable gold production (ca. 160 tons) by artisanal local miners (*garimpeiros*) (Paes de Barros, 2007). The AFGP is in the central-southern segment of the AC (north of the Mato Grosso state) and occurs as a NW-SE elongated belt over 500 km (Souza et al., 2005; Paes de Barros, 2007; Alves et al., 2019; Rizzotto et al., 2019), in the vicinity of Tapajós-Parima (2.03 – 1.88 Ga) and Rondônia-Juruena (1.82 – 1.54 Ga) tectonic-structural provinces (Santos, 2003; Santos et al., 2000, 2006).

The Province is majorly composed of Paleoproterozoic granite-volcanic sequences generated in an onset of magmatic arcs, which are covered by Quaternary alluvial sediments (Souza et al., 2005; Scandolara et al., 2017; Rizzotto et al., 2019; Alves et al., 2020; Trevisan et al., 2021). These units host innumerous medium to high-grade gold-rich placers and hydrothermal occurrences, especially in its easternmost and southeast sectors, along the NW-SE Peru-Trairão striking belt (Paes de Barros, 2007; Miguel-Jr, 2011; Assis et al., 2014; Bettencourt et al., 2016; Juliani et al., 2021; Mesquita et al., 2022).

Over the last three decades, significant advances in the geological and metallogenetic knowledge on province, initially promoted by Brazilian Geological Survey (Souza et al., 2005; Alves et al., 2019; Rizzotto et al., 2019), further supported by investments from mining companies focused on gold exploration (Paes de Barros, 1994, 2007; Moura et al., 2006; Assis et al., 2017). The improvements allowed understanding the importance of Paleoproterozoic calc-alkaline magmatic events concerning the ore-forming processes responsible for its gold occurrences (Moura, 1998; Assis et al., 2014, 2017; Duarte, 2015; Bettencourt et al., 2016; Juliani et al., 2021; Trevisan et al., 2021; Mesquita et al., 2022; Poggi et al., 2022). The hydrothermal-magmatic connection is highlighted in disseminated and vein-type gold occurrences housed by 1,97 – 1,77 Ga granites (Moura et al., 2006; Assis et al., 2014; Juliani et al., 2021; Trevisan et al., 2021). Nevertheless, there is a group represented by structurally-controlled gold occurrences, of great economic importance, whose geological descriptive attributes are ambiguous due share similarities with mesothermal and porphyry-epithermal gold systems (Santos et al., 2001; Poggi et al., 2022; Mesquita et al., 2022).

In order to shed more light on these discussions, this work reports the identification of the main descriptive features of the Aguinaldo structurally-controlled gold occurrence (Nova Guarita city, MT), such as its host rock, its U-Pb zircon age, the paragenetic evolution of its hydrothermal patterns and the ore zone, the nature of its quartz-rich veins, and the composition of chlorite and white mica from the hydrothermal halos. These data provide further discussions regarding the gold metallogeny that took place into the AFGP, especially if considered the ore-forming processes answerable for forming their structurally-controlled (filonar-type style) gold occurrences.

GEOLOGIC SETTINGS

The AFGP is in the central-south portions of AC (Brazil), where configures an WNW-SSE elongated belt of ca. 500 km (Paes de Barros, 2007; Miguel-Jr, 2011). The Province lies close to the boundaries of the Tapajós-Parima (2.03 – 1.88 Ga) and Rondônia-Juruena (1.82 – 1.54 Ga) tectonic provinces (Santos, 2003; Santos et al., 2000, 2006). It is mainly composed of Paleoproterozoic granite, volcanic, and volcano-sedimentary units, originated into an onset of continental arc magmatism that evolved toward to a post-collision setting, posteriorly covered by Mesoproterozoic continental sedimentary sequences and Quaternary alluvial sediments (Souza et al., 2005; Santos et al., 2006; Paes de Barros, 2007; Silva and Abram, 2008; Juliani et al., 2013, 2014, 2021; Carneiro et al., 2014; Assis, 2015; Scandolara et al., 2017; Alves et al., 2019; Rizzotto et al., 2019; Trevisan et al., 2021).

The Tapajós-Parima province comprises the Parima, Uaimiri, Tapajós and Peixoto de Azevedo domains (Santos, 2003; Santos et al., 2004). The latter encompasses the older units of the province, including Orosirian tonalitic to granitic gneiss with minor migmatite (ca. 2.03 – 1.97 Ga) of continental arc affinities, belonging to basement (Cuiú-Cuiú Complex) (Pessoa et al., 1977; Paes de Barros, 2007; Alves et al., 2020). This unit also includes calc-alkaline foliated I-type quartz-diorite, tonalite to granodiorite (Assis, 2015; Alves et al., 2020; Trevisan et. al., 2021) (Figure 1). These rocks are intruded by multiple 1.99 – 1.95 Ga undeformed syn-orogenic calc-alkaline oxidized and continental arc granites, represented by Pé Quente (1.99 – 1.97 Ga; Assis, 2015; Dezula, 2016; Rios, 2019) and Nhandu suites (1.96 – 1.95 Ga; Paes de Barros, 2007; Barros et al., 2015; Rocha, 2016; Alves et al., 2019), both from Juruena supersuite (Figure 1). Syn- to post-orogenic calc-alkaline, high-K, and I-type syenogranite, monzogranite, granodiorite, and tonalite, from Guarantã do Norte (1.9 Ga; Assis, 2015) and Matupá suites (ca. 1.88 – 1,86 Ga; Moura, 1998; Assis, 2015; Lima-Jr, 2017; Alves et al., 2019) were posteriorly emplaced. Subordinately, gabbro stocks and dykes (unknown age), from Flor da Serra suite, take place in easternmost segment of the Province (Souza et al., 2005; Paes de Barros, 2007; Miguel-Jr, 2011; Assis, 2015).

Porphyries, pyroclastic, volcano-sedimentary, and epiclastic I-type rocks from Colíder group (ca. 1.81 – 1,75 Ga), crosscut and lie over the previous units (Bini et al., 2015; Rios et al., 2018; Alves et al., 2019), together with alkaline A2-type granitoids, subvolcanics, and volcanics belonging to Teles Pires suite (1.79 – 1.75 Ga; Santos et al., 2000; Scandolara et al., 2017; Alves et al., 2019; Rizzotto et al., 2019).

Based on Re-Os pyrite and molybdenite ages, Assis et al. (2017) discuss the importance of the Colíder group as the magmatic event responsible for the formation of the granite-hosted gold-rich deposits of the AFGP, therefore, to its gold metallogeny.

Mesoproterozoic to Paleozoic clastic sedimentary sequences (Alto Tapajós basin), composed of quartz-sandstone, mudstone, siltstone, rhythmite, and local conglomerate, infrequently lateralized, overlain the units previously presented and represent an intracontinental rift basin (Alves et al., 2019). Quaternary alluvial fine to coarse-grained sand and polymictic gravel layers host gold-rich placer occurrences, also prospected by artisanal miners (Souza et al., 2005).

In this context, the Peixoto de Azevedo Domain hosts a variety of hydrothermal gold-rich occurrences (Alves et al., 2019; Juliani et al., 2021; Trevisan et al., 2021). Based on ore paragenesis and style, such mineralizations have been clustered as (i) disseminated, vein-type, and stockwork gold occurrences in 1.97 – 1.86 Ga calc-alkaline granites; (ii) vein-type and structurally-controlled gold occurrences housed in 2,05 – 1,97 Ga basement rocks; and (iii) polymetallic vein-type gold occurrences in 1,86 – 1,77 Ga granites, porphyries, and volcanics (Silva and Abram, 2008; Assis et al., 2014; Bettencourt et al., 2017; Juliani et al., 2021; Mesquita et al., 2022). Mineralizations from groups (i) and (iii) have been interpretated as similar to gold-porphyry and low to intermediate- sulfidation epithermal systems, whereas those belonging to group (ii) share features equivalent to porphyry and mesothermal gold deposits (Moura et al., 2006; Rodrigues, 2012; Trevisan, 2012, 2015; Bettencourt et al., 2016; Assis et al., 2017; Juliani et al., 2021; Mesquita et al., 2022; Poggi et al., 2022). Nevertheless, none mine company has achieved success in their exploratory mineral issues for applying the mesothermal model.

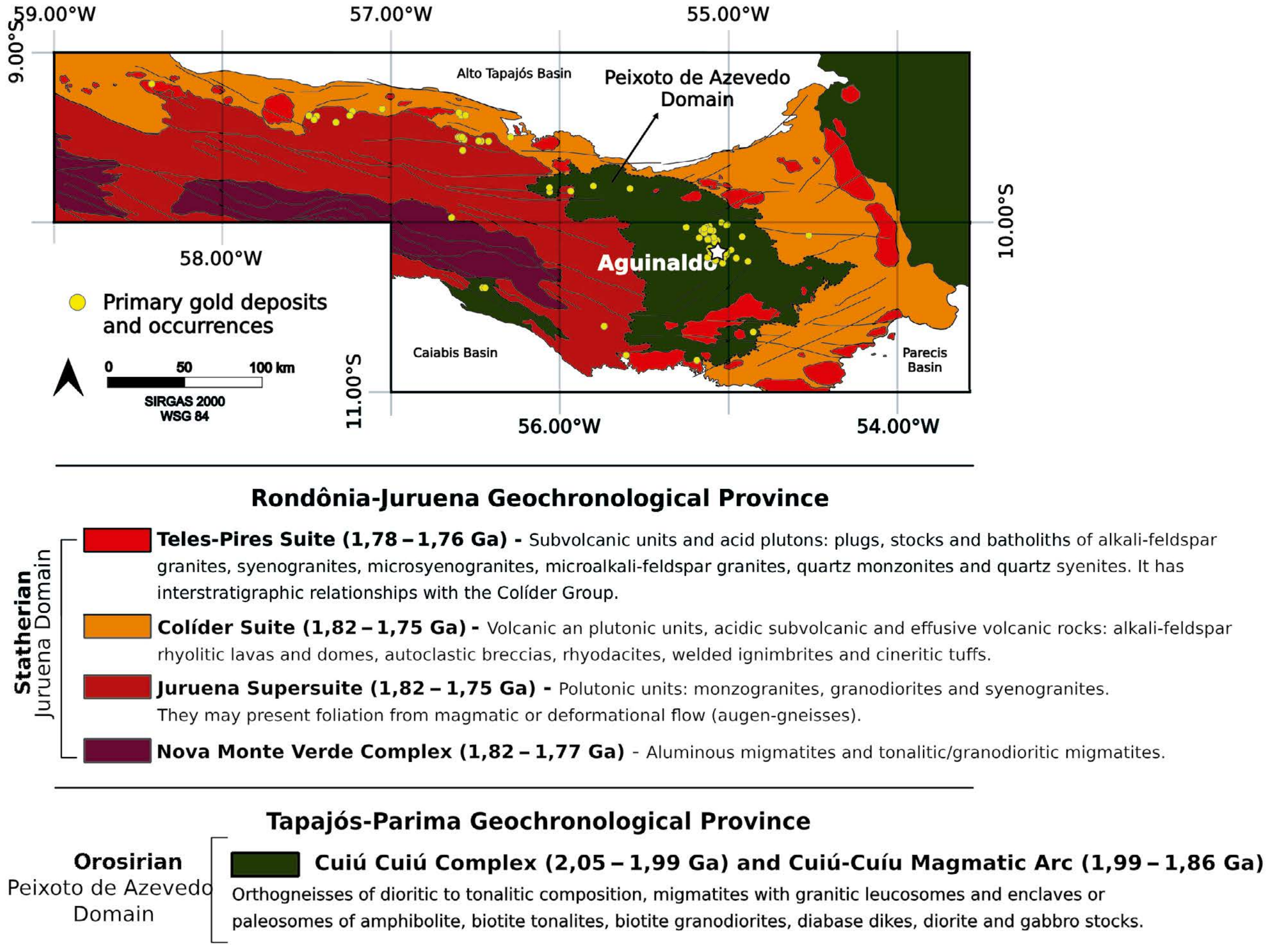

Modified from Rizzotto et al. (2019).

Figure 1. Simplified regional geological setting of the Alta Floresta Gold Province.

MATHERIALS AND METHODS

Sampling and Petrography

Sampling was conducted along the galleries of Aguinaldo occurrence, from mineralized quartz-veins, hydrothermal alteration halos, and portions of less intense modified-hydrothermally host rock. A total of 25 representative samples were selected to perform petrographic descriptions, geochronology, and mineral chemistry (chlorite and white mica). The thin sections preparation was performed at Instituto de Geociências, Universidade de São Paulo (IGc-USP).

The petrographic descriptions were carried out using a transmitted and reflected light Zeiss microscope (Axioskip 40 model), at Petrography Laboratory, at Universidade Estadual Paulista (UNESP), Instituto de Geosciências e Ciências Exatas (IGCE, Rio Claro-SP). This stage aimed the identification of (i) host rock composition, textures, and microstructures, (ii) paragenetic evolution concerning the hydrothermal alteration; (iii) ore styles and paragenesis; and (iv) chlorite and white mica (sericite and muscovite) textures.

Petrography was detailed in Scanning Electron Microscope (SEM), at Scanning Electron Microscope Laboratory, UNESP. The SEM allowed the recognizance of minor mineral phases not individualized during the transmitted and reflected light petrography, eventual zoning in sulfides, replacement and intergrowth textures in chlorite and white mica, besides the silver contents in gold. The mineral abbreviation is in accordance with Silvola and Schmid (2007).

Mineral Chemistry

Mineral chemical composition was obtained on representative hydrothermal chlorite, sericite, and muscovite, using the JEOL JXA-8230 Electron Microprobe (EMP), from Electron Microprobe Laboratory (IGCE-UNESP), operated with a 15 kV voltage, 20 nÅ current, and a 3 μm spot size beam. The following standards were used as calibration: orthoclase (for Si and K), anorthite (for Al), albite (for Na), wollastonite (for Ca), ilmenite (for Fe and Ti), diopside (for Mg), rhodonite (for Mn), chromite (for Cr), barite (for Ba), sodalite (for Cl), and synthetic Ni-rich oxide (for Ni). The EMP allowed obtaining the concentrations of the major elements (Si, Al, K, Na, Mg, Fe, Ti, Ba, Cr e Mn), besides Ba, Cl, Cr as trace elements (in ppm).

A total of 91 analyses were performed on muscovite, 65 on chlorite, and 18 on sericite (totalizing 174 analysis points). The data were processed using the AX® (for white mica) and WinCcac® (for chlorite) softwares. The diagrams here presented obtained in ioGAS™ software, then, vectored in CorelDRAW® Graphics Suite 2020 software.

Zircon SHRIMP U-Pb isotope analysis

One representative sample (AGRB15) from less-intense hydrothermally altered gneiss was analyzed by U-Pb Sensitive High Resolution Ion Microprobe (SHRIMP IIe) zircon method, at Laboratory of High-Resolution Geochronology (GeoLab), located at IGc-USP. Zircon crystals concentration was carried out at the Geochronological Research Center (CPGeo), from IGc-USP. The zircon concentration was initially obtained crushing the sample with a Fritsch Jaw crusher, then, grounded it using a metal disc mill, and the separation of heavy minerals on a vibrating table. The paramagnetic minerals were extracted from heavy minerals concentration employing a Sm-Nd magnet. Heavy minerals concentrate of <350 μm fraction were magnetically individualized by Frantz applying gradual current increasing of 0.1A, 0.3A, 0.6A, 1.0A and 1.5A. Non-magnetic heavy minerals (e.g. zircon, apatite) were concentrated by using heavy liquid density separation. Inclusion-free zircons from non-magnetic fraction were then handpicked under binocular ZEISS lens.

The final zircon concentrate was sent to GeoLab, where it was manually mounted in epoxy mounts resin and polished with diamond paste to expose their internal structures. Furthermore, TEMORA external standard (Black et al., 2004) was mounted together with the obtained zircon concentration, for normalizing the isotopic fractionation during the analyses of zircon crystals. To further target the inner areas during the U-Pb isotopic analyses, the polished mount was imaged with a FEI-QUANTA 250 Scanning Electron Microscope equipped with secondary-electron (SEM) and cathodoluminescence (CL) detectors. The cathodoluminescence operation conditions were: 60 μm of emission current, 15.0 kV of acceleration voltage, 7 μm of beam diameter, and 200 μs of acquisition time. The correction of common Pb was based on ^{204}Pb measured (the ^{206}Pb/^{238}U ratio is less than 2%), whereas the uranium abundance and U/Pb ratios were calibrated against TEMORA standard.

The typical error component for the ^{206}Pb/^{238}U ratio was less than 1.2%, whereas for ^{207}Pb/^{206}Pb and ^{207}Pb/^{235}U ratios were less than 2.12 and 2.8%, respectively. The spot size applied was of 30 μm. Concordia age calculation was given by using ISOPLOT© 3.0 (Ludwig, 2003). The data exhibits 95% confidence limit and the uncertainties for each individual analysis are expressed by 2σ.

GEOLOGY OF THE AGUINALDO GOLD OCCURRENCE

Host rock

The Aguinaldo occurrence places ca. 30 km northeast of the Nova Guarita (MT) city, and comprises an area of nearly 7000 hectares, at the alluvial flood plain of the Peixoto river. Its gold production came from both gold-rich placer hosted by gravel layers, as from quartz-sulfide veins housed in metamorphic basement.

The host rock is a gray-to-greenish, porphyroblastic mylonite gneiss, moderately magnetic, anisotropic, and medium to coarse-grained. The porphyroblastic texture is represented by 1 – 2 cm long reddish and stretched K-Feldspar crystals that comprise ca. 20 – 30% of rock volume (Figure 2A). Moreover, its quartz-feldspar-rich gneissic banding is intercalated by a fine-grained matrix composed of chlorite, sericite, and ankerite (Figure 2B), besides a well-defined mylonitic foliation defined by mineral stretching and comminuting (Figure 2C). Magnetite, apatite, zircon, and allanite are accessory phases, whereas muscovite, sericite, ankerite, calcite, pyrite, and chalcopyrite correspond to hydrothermal minerals (Figures 2D-2F).

Hydrothermal alteration temporal sequence

The mylonite gneiss is variably affected by distinctive pervasive hydrothermal alterations, for which the temporal evolution sequence is defined as (1) initial albite-rich alteration; (2) potassic alteration with K-Feldspar; (3) sericite-muscovite alteration; (4) silicification and silica infills; (5) pervasive carbonate alteration and minor calcite in veinlets; (6) chlorite alteration; and (7) late silica infills (Figure 3).

The pervasive albite-rich alteration represents the initial hydrothermal stage and consists of albite ± quartz (Figure 4A) that overprinted the igneous feldspar crystals, and it is usually distal to quartz-ore veins. The albite is fine to medium-grained, sub-idiomorphic to xenomorphic, and occasionally exhibits the chessboard texture.

The pervasive potassic alteration is defined by K-Feldspar ± quartz ± hematite ± magnetite assemblage, responsible for the reddish color of mylonite gneiss (Figures 2A and 4B). This stage is further observed distally to quartz-ore veins, in sectors where is less intensively obliterated by subsequent alterations. The igneous feldspar crystals and hydrothermal albite are often partial to integrally replaced by K-Feldspar, resulting in overgrowth edges. Very fine-grained hematite occurs as inclusion in K-Feldspar.

The sericite-muscovite alteration represents the most intense hydrothermal stage since it can completely overprint the matrix and textures of the mylonite gneiss (Figure 4C), resulting in its light-greenish color. It is represented

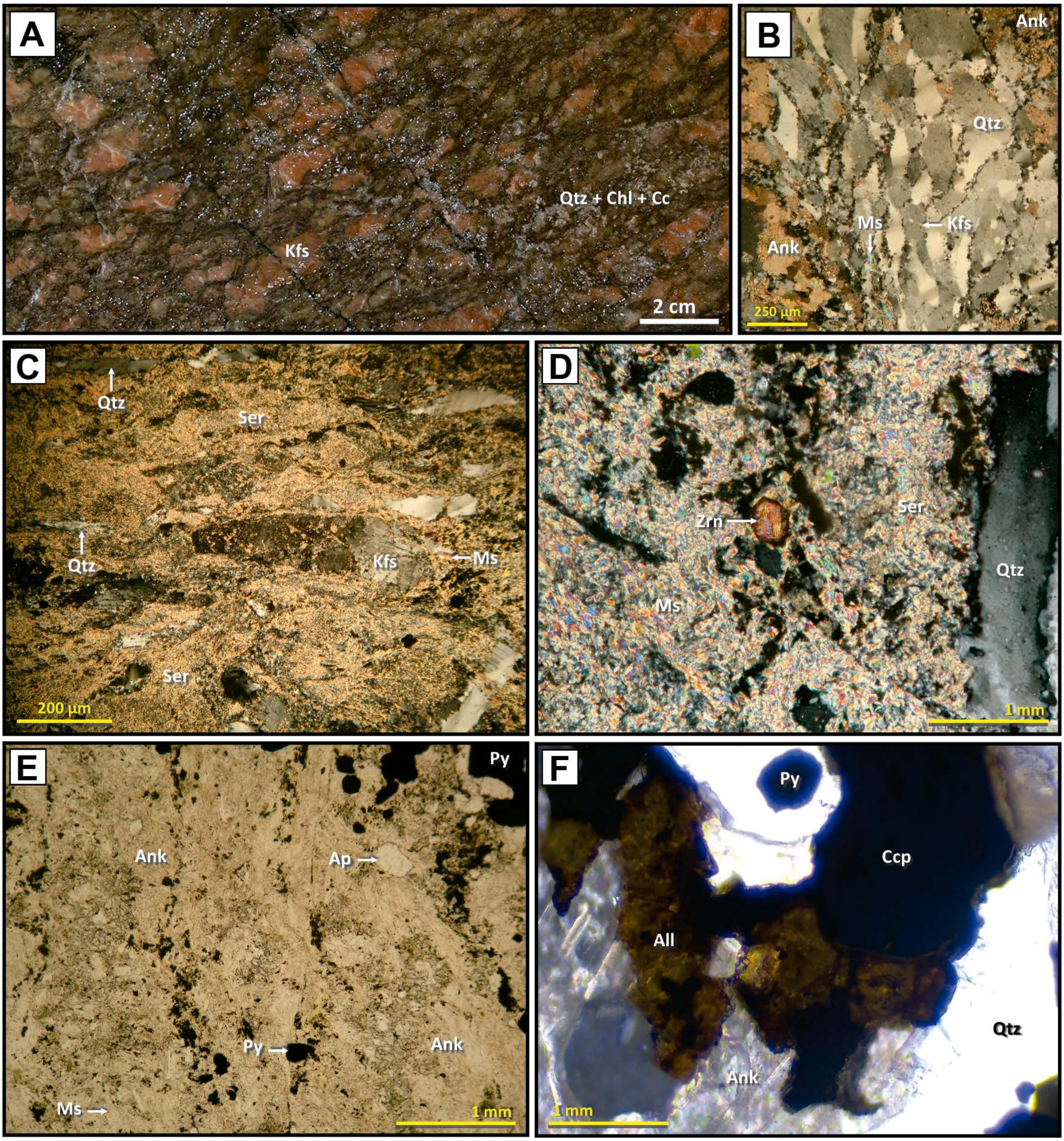

Fhotomicrographs: (B-D,F) Cross-polarized transmitted-light; and (E) Plane-polarized transmitted-light.
Mineral abbreviations: (Ank) ankerite, (All) allanite, (Ap) apatite, (Cc) carbonate, (Ccp) chalcopyrite, (Chl) chlorite, (Kfs) K-Feldspar, (Ms) muscovite, (Py) pyrite, (Qtz) quartz, (Ser) sericite, (Zrn) zircon.

Figure 2. Petrographic features identified in mylonite gneiss: (A) The anisotropy is defined by reddish fine to coarse-grained stretched K-Feldspar porphyroblasts in a matrix mainly composed of quartz, carbonate, and chlorite; (B) The fine coarse-grained quartz from gneissic banding is often stretched by mylonite-deforming processes; (C) K-Feldspar porphyroblasts partially obliterated by hydrothermally altered matrix represented by fine-grained quartz, muscovite, and sericite; (D) Coarse-grained magmatic euhedral zircon into the sericite + muscovite alteration; (E) Fine-grained magmatic subhedral apatite in the assemblage consisting of ankerite, muscovite, and minor pyrite; (F) Coarse-grained magmatic subhedral allanite partially altered by hydrothermal ankerite.

by sericite + muscovite ± quartz ± pyrite paragenesis better developed closely to vein-type ore.

The silica injection occurs as veins-controlled quartz, in both (i) quartz-dominated veins with variable sulfide contents (Figure 4D), such as sulfides gold-bearing veins, and (ii) quartz ± ankerite ± dolomite barren veins, in which sulfide minerals are absent. Collectively, this stage is defined by 0.5 – 1.5 m parallelized veins with local thinner

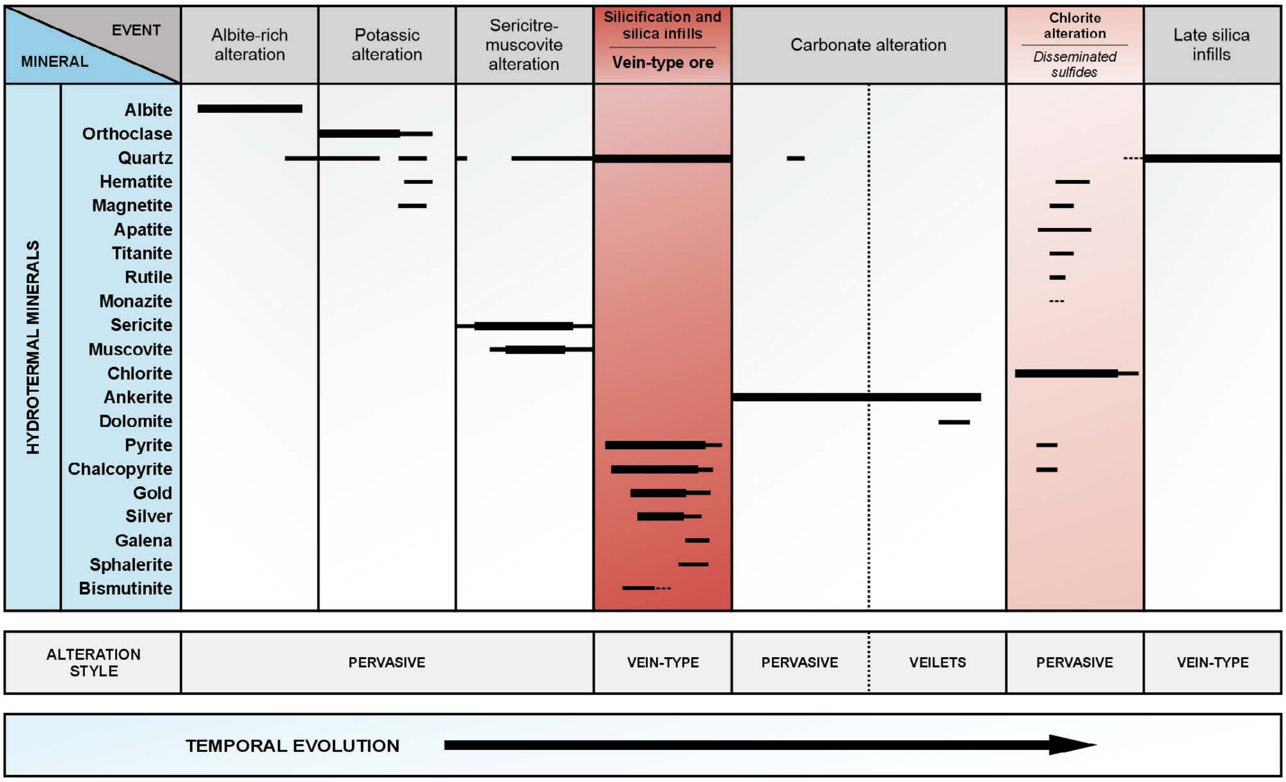

Figure 3. Paragenetic sequence and mineral association of hydrothermal alteration and mineralization suggested for Aguinaldo gold occurrence.

segments (pinch and swell geometry?), and comb-quartz texture. Quartz is medium to coarse-grained, xenomorphic, and exhibits low to moderate undulatory extinction. Ankerite and dolomite occur less than 10% in veins volume, are mainly sub-idiomorphic, and medium-grained.

The carbonate alteration corresponds to an expressive hydrothermal stage that envelops the gold-bearing veins. It is characterized by the pervasive calcite + ankerite ± dolomite paragenesis commonly (Figure 4E), although fracture-controlled veinlets (up to 0.1 mm thick) can also occur. It is intensively related to igneous plagioclase and hydrothermal albite replacement, in addition to obliterating the sericite-muscovite alteration.

The chlorite alteration overprints the previous alterations sequence and is dominated by fine-grained chlorite (Figure 4F), despite subordinated hematite, magnetite, apatite, titanite, rutile, monazite, pyrite, and chalcopyrite. It represents an extensive pervasive alteration halo, more intensive toward the ore zone. Pyrite, chalcopyrite, and hematite are disseminated in minor amounts (2 – 4% vol.), especially close to vein-type ore. Pyrite is sub-idiomorphic, chalcopyrite is xenomorphic, and both form fine to medium-grained crystals. Fine-grained idiomorphic to sub-idiomorphic magnetite is restricted to chlorite veinlets. Apatite is dispersed in the chlorite-rich zones, as idiomorphic fine to medium-grained crystals. Nevertheless, hematite occurs as xenomorphic fine-grained grains, usually replacing pyrite.

Fracture-controlled barren quartz veinlets represent the final stage concerning the hydrothermal paragenetic sequence identified at Aguinaldo occurrence. It corresponds to gold, silver, and sulfide-free quartz veinlets.

Gold mineralization

The entire gold-bearing zone at Aguinaldo occurrence is structurally-controlled by NNE-SSW parallel quartz + sulfides ± carbonate veins (from 0.5 – 1.5 m thick) that are cogenetic to silica infills stage (Figures 3 and 5A). Based on paragenesis, the sulfide veins can be clustered as (i) quartz + sulfides ± ankerite ± dolomite gold-bearing vein, with sulfide paragenesis composed of chalcopyrite (60 – 80%), pyrite (20 – 40%), bismuthinite (<2%), sphalerite (1 – 2%), galena (~1%), and silver (<1%) (Figure 5A); and (ii) quartz ± ankerite ± dolomite barren vein, with minor pyrite ± chalcopyrite ± silver ± sphalerite ± galena ± bismuthinite. The former exhibits high to massive (up to 80% in volume) sulfide concentration, whereas the barren vein shows low volume (<5%) in sulfide. Furthermore, covellite, digenite, and goethite are common in both situations, replacing chalcopyrite and pyrite (Figure 5A), resulting from supergene conditions.

Chalcopyrite is xenomorphic, medium to coarse-grained, and occurs enclosing the pyrite and filling its fractures and interstices (Figures 5A, 5B and 5D). Pyrite usually manifests itself in lower concentrations, as fine to

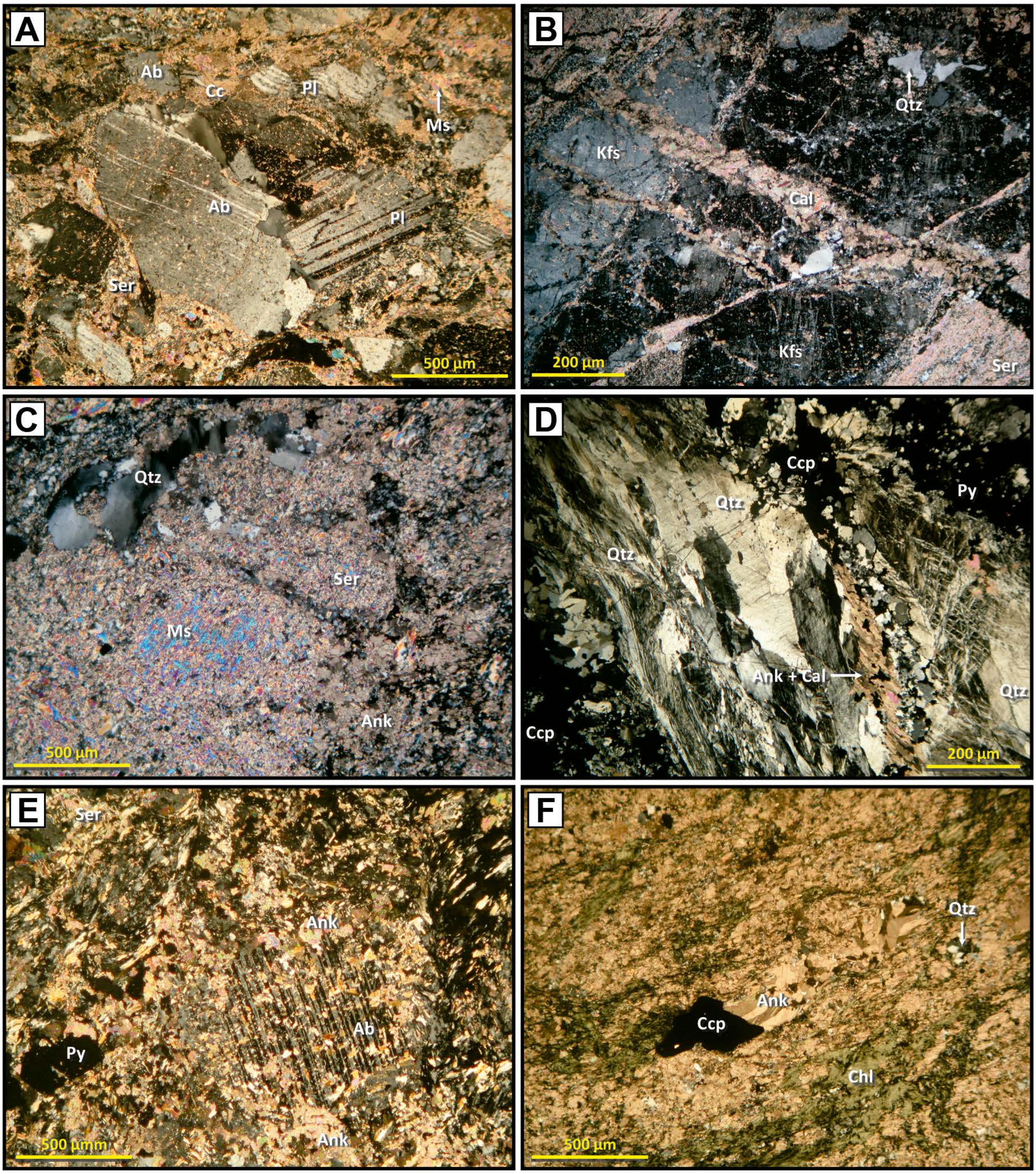

Photomicrographs: A-F: Cross-polarized transmitted light.
Mineral abbreviations: (Ab) albite, (Ank) ankerite, (Cal) calcite, (Cc) carbonate (calcite?), (Ccp) chalcopyrite, (Chl) chlorite, (Kfs) K-Feldspar; (Ms) muscovite; (Pl) plagioclase, (Py) pyrite, (Qtz) quartz, (Ser) sericite.

Figure 4. Major petrographic features concerning the hydrothermal paragenetic sequence of Aguinaldo gold occurrence: (A) Pervasive albite alteration overprinted by sericite-muscovite and carbonate alterations, with slight deformation of igneous albite twinning; (B) Coarse-grained K-Feldspar partially replaced by sericite and crosscut by calcite-rich veinlet; (C) Igneous plagioclase completely pseudomorphed by hydrothermal sericite and muscovite closely to ore zone; (D) Intense mylonite-deformed and recrystallized quartz forming quartz sub-grains texture from quartz, besides interstitial fine-grained pyrite and chalcopyrite and late ankerite + calcite veinlet; (E) Extensive carbonate alteration obliterating igneous albite previous and partially replaced by sericite; (F) Chlorite-dominated alteration overprinting ankerite from carbonate alteration, proximally to ore zone.

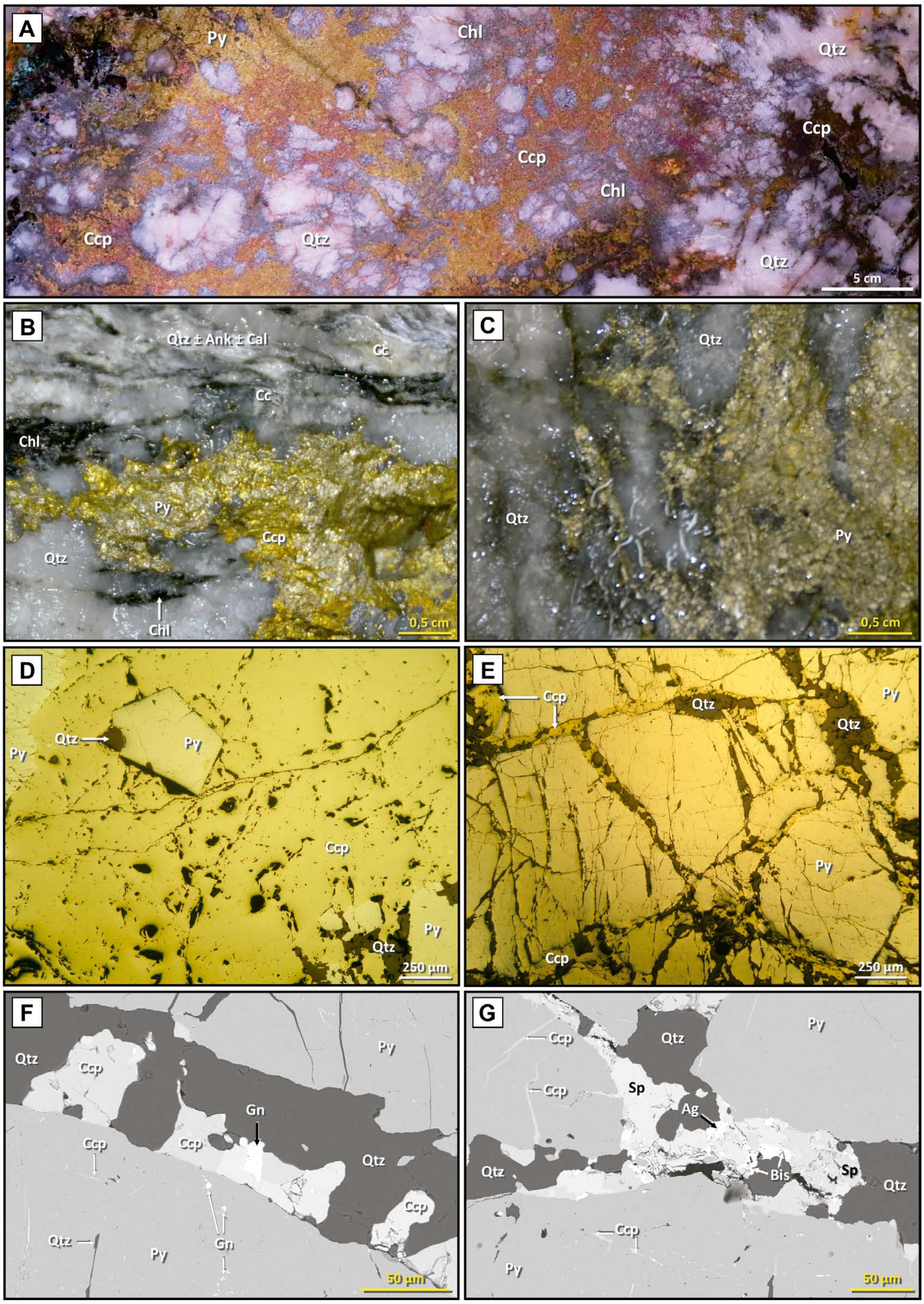

Photomicrographs: (D-E) Plane-polarized reflected light; (F-G) Backscattered electron images.
Abbreviations: (Ag) silver; (Ank) ankerite; (Bis) bismuthinite; (Cal) calcite; (Cc) carbonate; (Ccp) chalcopyrite; (Chl) chlorite; (Gn) galena; (Qtz) quartz; Sp (sphalerite).

Figure 5. Main features and petrographic related to ore-zone from Aguinaldo gold occurrence: (A) Vein-type ore composed of fragmented quartz as in sub-grains texture with interstitial chalcopyrite and chalcopyrite (ca. 45% in volume), the latter incipiently oxidized by covellite; (B) Pyrite and chalcopyrite in quartz ± carbonate vein with deformed comb-quartz texture delimited by fine-grained chlorite, as observed at upper portion of figure; (C) Idiomorphic to sub-idiomorphic and fine to coarse-grained pyrite-dominated zone in quartz vein; (D) Xenomorphic medium to coarse-grained massive chalcopyrite with fine to medium-grained pyrite and minor quartz inclusions; (E) Fine-grained chalcopyrite and quartz filing fractures and interstices in the massive, coarse-grained pyrite zone; (F) Xenomorphic and fine-grained chalcopyrite, galena and quartz filling fracture in pyrite with small flames of chalcopyrite and blebs of galena; (G) Xenomorphic and fine-grained sphalerite, silver, bismuthinite, and quartz association that fill interstices among pyrite with chalcopyrite inclusions.

coarse-grained idiomorphic to sub-idiomorphic crystals, or crystal agglomerates (Figures 5B – 5E, and 6A, 6B), eventually with small inclusions of quartz and covellite. Sphalerite forms diminutive inclusions in chalcopyrite, whereas galena, bismuthinite, and silver within pyrite (Figures 5F and 5G).

Gold forms rounded to subrounded inclusions (≤ 75 μm), occupies the edges (Figure 6A), and fills fractures mainly in pyrite (Figure 6B). Occasionally, gold can also be included in and/or close to sphalerite (Figure 6C), and filling fractures in chalcopyrite (Figures 6B and 6D). Low to moderate silver contents (up to 43%) were identified in electrum (Au-Ag alloy). Silver performs sub-rounded to xenomorphic inclusions in chalcopyrite (Figure 5G). In addition, bismuthinite is often included in pyrite, chalcopyrite, and sphalerite, especially associated with gold and silver.

Furthermore, in barren sulfide-rich veins, pyrite (65 – 80%) predominates over chalcopyrite (20 – 35%), silver, sphalerite, galena, and bismuth-bearing minerals occur in minor amounts, and gold is absent. Pyrite is majorly sub-idiomorphic, medium to coarse-grained, and essentially forms crystal clusters. Chalcopyrite fills the pyrite interstices and eventually occurs as small inclusions in quartz and pyrite. Sphalerite shows silver and bismuth-bearing minerals inclusions, whereas galena is included in chalcopyrite.

Mineral Chemistry

Chlorite

A total of 65 analyses were performed in three chlorite textures: interstitial chlorite (n=31), veinlet-type chlorite (n=19), and chlorite as agglomeration (n=15). The compositional average for each chlorite textural variety is shown in Table 1 (for SiO_2, Fe_2O_3, MgO, Al_2O_3, TiO_2, K_2O and Na_2O as wt.%). The chlorite composition data were recalculated based on 14 oxygen atoms per formula unit (a.p.f.u.). Due to the anomalous SiO_2 contents (> 34.0 wt.%), a total of 11 analyses from interstitial chlorite and three from chlorite as agglomeration textures were discarded from the dataset.

The interstitial chlorite shows homogeneous SiO_2

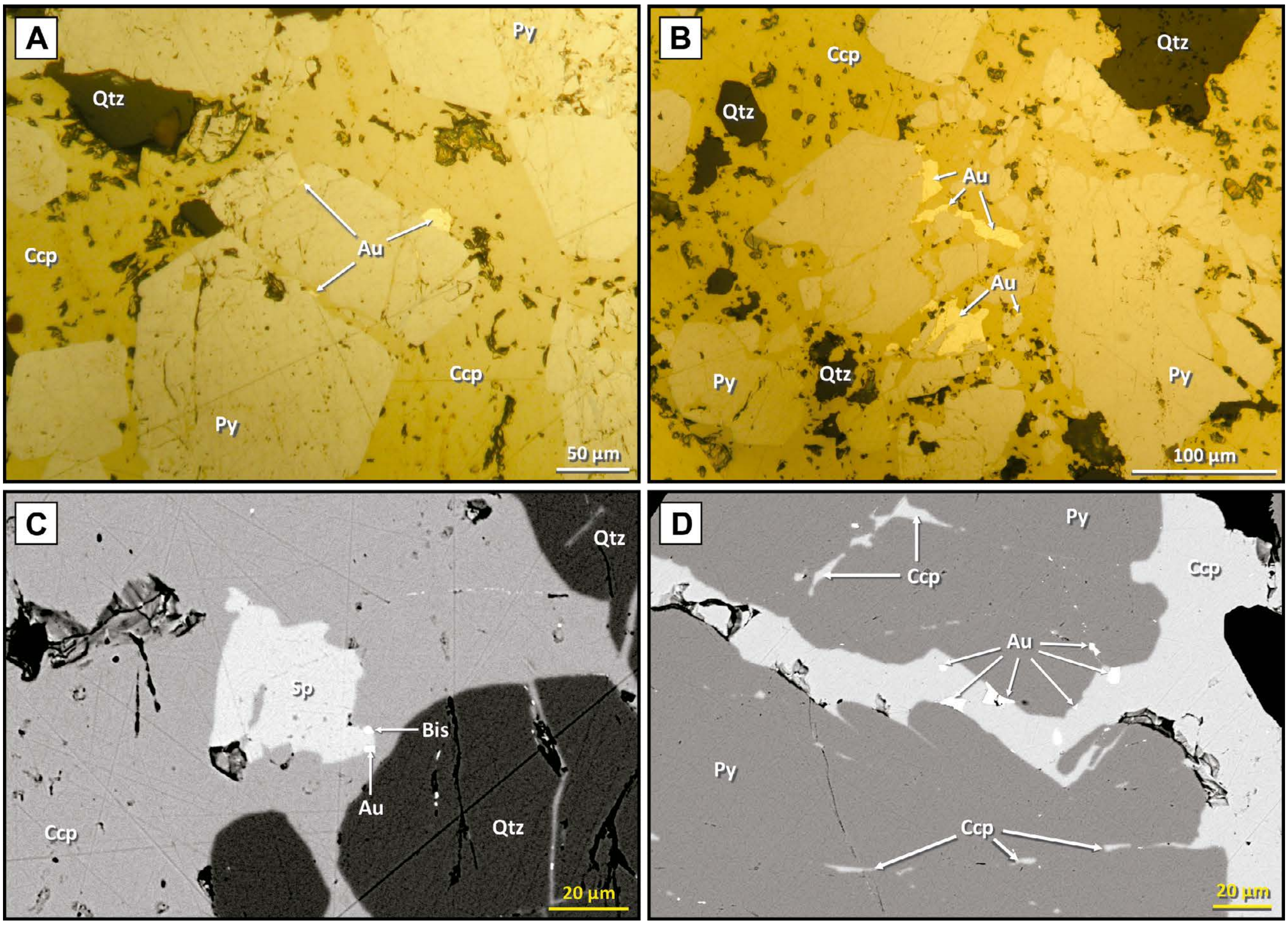

Photomicrographs: (A-B) Plane-polarized reflected light; and (C-D) Backscattered electron (BSE) images.
Abbreviations: (Au) gold; (Bis) bismuthinite; (Ccp) chalcopyrite; (Py) pyrite; (Qtz) quartz; (Sp) sphalerite.

Figure 6. Modes of occurrence and mineral association of gold at Aguinaldo: (A) Subangular to sub-rounded and very-fine-grained gold grains at pyrite edges and, in turns, included in chalcopyrite; (B) Xenomorphic gold grains included in chalcopyrite and overgrowing pyrite; (C) Very-fine-grained gold and bismuthinite in edges of xenomorphic sphalerite, which is encompassed by chalcopyrite, in quartz vein; (D) Bordering and interstice-filling chalcopyrite over chalcopyrite-bearing gold as xenomorphic small inclusions.

Table 1. Composition average for the chlorite textures identified at Aguinaldo gold occurrence (n=65).

Elements (wt.%)	Chlorite textures		
	Interstitial (n = 31)	Veinlet--type (n = 19)	Agglomeration (n = 15)
SiO_2	27.79	28.28	27.71
Fe_2O_3	20.64	17.44	19.57
MgO	19.70	21.82	20.60
Al_2O_3	18.95	18.51	18.83
TiO_2	0.02	0.021	0.035
K_2O	0.094	0.041	0.057
Na_2O	0.032	0.039	0.057

(25.05 – 29.51 wt.%) and Al_2O_3 (17.8 – 21.1 wt.%) values, heterogeneous Fe_2O_3 (16.6 – 30.2 wt.%) and MgO (12.6 – 22.8 wt.%) contents, however, low Na_2O (0.01 – 0.08 wt.%), TiO_2 (0.01 – 0.09 wt.%) and K_2O (0.01 – 0.57 wt.%) concentrations.

The analyses performed on veinlet-type chlorite have returned more restrictive SiO_2 (26.6 – 28.6 wt.%), Al_2O_3 (17.6 – 20.3 wt.%), MgO (19.6 – 21.6 wt.%) and Fe_2O_3 (19.1 – 20.7 wt.%) values, besides low K_2O (0.02 – 0.12 wt.%), Na_2O (0.03 – 0.23 wt.%) and TiO_2 (0.01 – 0.09 wt.%).

In sequence, the chlorite as agglomeration presents higher SiO_2 (22.2 – 29.2 wt.%) values, homogeneous MgO (19.1 – 22.9 wt.%), Fe_2O_3 (16.1 – 20,1 wt.%) and Al_2O_3 (17.7 – 20.1 wt.%) contents, and over again, low Na_2O (0.01 – 0.12 wt.%), K_2O (0.01 – 0.07 wt.%), and TiO_2 (0.01 – 0.03 wt.%) concentrations.

Based on chlorite classification ternary, proposed by Zane and Weiss (1998), the hydrothermal chlorite from Aguinaldo is extensively trioctahedral (Type I), although, clustering into two groups: (i) Mg-chlorite (clinochlore): framing essentially the veinlet-type chlorite and chlorite as agglomerations, and (ii) Fe-chlorite (chamosite): concentrating the interstitial chlorite (Figure 7A).

Foster (1962) proposed the Fe/(Fe+Mg) ratios as a chemical index useful in identifying chlorite composition. Therefore, according to the Fe/(Fe+Mg) ratios vs. Al^{IV} diagram, the chlorite dataset majorly falls into the brunsvigite field, although the increase in Al^{IV} values results in a linear trend toward the ripodolite field (Figure 7B), exclusively for interstitial chlorite.

Moreover, a strongly negative correlation between FeO and MgO contents (Figure 7C) is observed in the chlorite EPMA dataset from Aguinaldo, suggesting Tschermak replacement between Fe^{2+} and Mg^{2+} at the octahedral site.

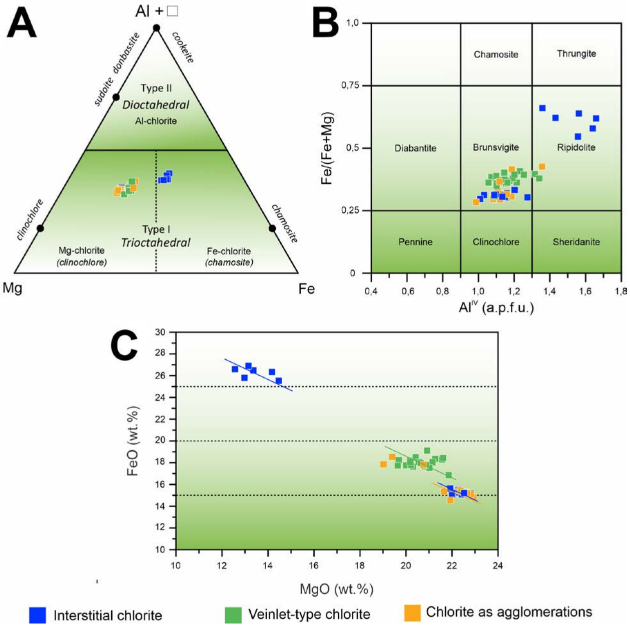

Figure 7. Compositional classification diagrams for chlorite textures from Aguinaldo occurrence according to: (A) Zane and Weiss (1998); (B) Foster (1962); and (C) Tschermak replacement based on MgO (wt.%) versus FeO (wt.%).

Additionally, anew it is noted the existence of both Fe-rich chlorite, mainly composed of interstitial chlorite, and Mg--rich chlorite, essentially represented by those that occur as agglomeration of grains and in veinlets. Such clustering agrees with the chlorite classification proposed by Zane and Weiss (1998), as previously presented.

White Mica

The white mica dataset summarizes 109 analyses, derived from eight textures: agglomeration of muscovite (n=25), coarse-grained muscovite (n=23), pervasive sericite (n=17), veinlet-type muscovite (n=16), sub-idiomorphic muscovite (n=14), interstitial muscovite (n=16), radial muscovite (n=07), and pseudomorph sericite (n=01). The data were recalculated based on 11 oxygen atoms per formula unit (a.p.f.u.). Table 2 summarizes the composition average achieved for each white mica texture, concerning the SiO_2, Al_2O_3, K_2O, Fe_2O_3, MgO, TiO_2, and Na_2O values.

Upon examination of the entire dataset, nine analytical points were excluded due to their anomalous composition values: one data from agglomerate of muscovite for exhibiting high TiO_2 values (>9.0 wt.%), one from interstitial muscovite for displaying dissonant SiO_2 (<35.0 wt.%), Fe_2O_3 (>16.0 wt.%), MgO (>11.0 wt.%) and H_2O (>10.0 wt.%) contents, three from coarse-grained muscovite for showing anomalous H_2O contents (3.0 wt.% < H_2O > 8.0 wt.%), and four from vein-type muscovite due their atypical SiO_2 (<44.0 wt.%), TiO_2 (>10.0 wt.%) and H_2O (<3.0 wt.% H_2O > 8.0 wt.%) contents.

The chlorite EMPA analyses on the eight white mica textures reveal uniform and homogeneous compositions.

Table 2. Composition average for the white mica textures identified at Aguinaldo gold occurrence.

Elements	Muscovite and sericite textures							
(wt.%)	Coarse-grained	Agglomeration	Sub-idiomorphic	Radial	Interstitial	Veinlets	Pervasive	Pseudomorph
SiO_2	47.99	48.18	48.07	48.72	48.71	48.69	48.21	48.82
Al_2O_3	30.28	30.36	29.46	30.41	31.24	31.64	30.45	30.16
K_2O	9.64	9.71	9.76	9.79	9.78	9.48	9.73	10.00
Fe_2O_3	4.59	4.11	5.19	3.65	3.41	2.76	4.01	3.56
MgO	2.07	1.99	2.20	2.10	2.20	2.29	2.00	2.31
TiO_2	0.31	0.25	0.40	0.21	0.25	0.24	0.20	0.05
Na_2O	0.18	0.15	0.16	0.20	0.18	0.20	0.16	0.12

The SiO_2 contents range from 46.02 – 49.84 wt.%, the Al_2O_3 from 26.67 – 32.86 wt.%, the K_2O from 7.66 – 10.28 wt.%, Fe_2O_3 from 2.07 – 6.09 wt.%, MgO from 1.28 – 2.86 wt.%, TiO_2 from 0.04 – 0.68 wt.%, and Na_2O are between 0.09 – 0.25 wt.%.

Nevertheless, the vein-type muscovite exhibits heterogeneous Fe_2O_3 (1.89 – 5.98 wt.%), besides higher MgO (1.68 – 5.33 wt.%) and TiO_2 (0.15 – 0.67 wt.%) values compared to other textures, whereas the sub-idiomorphic muscovite returned merely higher TiO_2 (0.12 – 0.55 wt.%) concentrations. Furthermore, higher Na_2O values were registered for radial muscovite (0.16 – 0.24 wt.%), interstitial muscovite (0.16 – 0.21 wt.%), and pseudomorph sericite (ca. 0.12 wt.%).

The geochemical homogeneity obtained for white mica reflects its composition closely aligned with the muscovite composition, if considered the muscovite-phengite compositional trend proposed by Deer et al. (1992) (Figure 8A). Based on K-Fe/(Fe+Mg)-Mg(Fe+Mg) ternary suggested by Tappert et al. (2013), the dataset fits into the Fe-Al caledonite field (Figure 8B). Moreover, it is highlighted that the muscovite and sericite from Aguinaldo occurrence can be clustered into three main groups: (i) coarse-grained and agglomerate of muscovite are closer to Fe-Al caledonite, whereas (ii) sub-idiomorphic muscovite and pervasive sericite display an intermediate composition from Fe-Al and Al-caledonite, and (iii) pseudomorph sericite, and the radial, interstitial, and vein-type muscovite fit closer to the Al-caledonite (Figure 8B).

The chemical homogeneity obtained for white mica is also observed in Tschermak substitution reactions. The strong negative correlation (R^2 = -0.97) between the octahedral site (Al^{IV}) and Si+(Fe+Mg) contents suggests cation substitution (Figure 8C), which is also detected on replacement equation $Al_{(t)} \rightarrow [Si: +(Fe^{2+}+Mg^{2+})]$, due its very strong negative correlation (R^2 = 0.84) (Figure 8D).

Chlorite geothermometer

The empirical chlorite geothermometers proposed by Cathelineau and Nieva (1985), Kranidiotis and MacLean (1987), Jowett (1991), and Zang and Fyfe (1995) were applied focusing on obtaining the Aguinaldo chlorite temperature formation.

The highest temperatures were obtained using the Jowett (1991) equation, as follows: interstitial chlorite (295 – 420º C); chlorite as agglomerations (283 – 378º C); and veinlet-type chlorite (308 – 360º C). The estimated intermediate temperatures were performed for adopting the Kranidiotis and MacLean (1987) and the Zang and Fyfe (1995) equations. The first returned such temperatures: interstitial chlorite (274 – 370° C), agglomeration of chlorite grains (266 – 334° C), and veinlet-type chlorite (285 – 320° C), whereas the former resulted in: interstitial chlorite (261 – 316° C), chlorite as agglomerations (253 – 307° C) and veinlet-type chlorite (266 – 298° C). Conversely, the Cathelineau and Nieva (1985) geothermometer equation indicates the lowest temperature ranges: interstitial chlorite (250 – 328º C); agglomeration of chlorite grains (242 – 304º C); and veinlet-type chlorite (258 – 292º C).

White mica geobarometer

Geobarometric estimates based on muscovite and sericite compositions were calculated according to the Massonne and Schreyer (1987) equation, analytically expressed by Anderson (1996) (Equation I). The chlorite temperature mode (ca. 314° C), based on the Jowett (1991) geothermometer, was considered for calculating the pressure (Equation II), since its more precise chemical parameters: (i) the correction factor index is expressed as Fe/(Fe+Mg); (ii) it is based on 14 oxygen atoms;

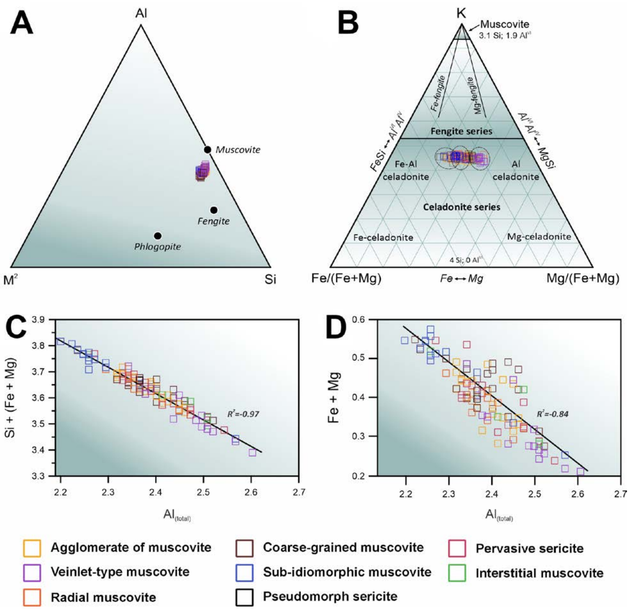

Figure 8. Compositional classification diagrams for white mica textures identified at Aguinaldo occurrence according to (A) Deer et al. (1992); and (B) Tappert et al. (2013); besides, binary correlation diagrams (C) $Al_{(total)}$ versus Si+(Fe+Mg); and (D) $Al_{(total)}$ versus (Fe+Mg). Legend: $M^2 = Fe^{2+}+Mg^{2+}+Mn^{2+}$; R^2 = Pearson correlation coefficient.

and (iii) the usage of tetrahedral aluminum (Al^{IV}) rather a silica (Si^{IV}) (Yavus et al., 2015).

$$P(Kbar) = -2{,}6786 \times Si^2 + 43{,}975 \times Si + 0{,}001253 \times T(°C) - 113{,}9995 \qquad 1$$

$$\text{where, } T(°C) = 319 \times [Al\overset{IV}{\underset{O_{14}}{}} + (0{,}1 \times \frac{Fe}{Fe+Mg})] - 69 \qquad 2$$

Collectively, the pressure estimates range from 0.14 – 1.84 kbar. In this scenario, the agglomeration of muscovite crystals returned pressures from 0.14 – 1.84 kbar, the pervasive sericite from 0.16 – 1.47 kbar, and the radial muscovite from 0.24 – 1.36 kbar. Lower values were obtained from coarse-grained muscovite (0.35 – 1.15 kbar), sub-idiomorphic muscovite (0.14 – 1.17 kbar), interstitial muscovite (0.30 – 0.94 kbar), and veinlet-type muscovite (0.22 – 0.96 kbar). The pressure for pseudomorph sericite was calculated from a single analysis (ca. 1.12 kbar).

GEOCHRONOLOGY: U-Pb RESULTS

A concentrate of zircon crystals was extracted from one sample collected from orthogneiss mylonite (AGRB-15).

The crystals are mainly light brown, idiomorphic, prismatic to oval-shaped, and exhibit lengths ranging from 95 to 217 μm (Figure 9). The cathodoluminescence images (CL) indicate well-developed magmatic oscillatory zoning, usually with more luminescent cores. Furthermore, the crystals reveal small fractures and rare mineral inclusions. Xenocrystic cores were identified in a few crystals, therefore, which were not analyzed for geochronology issues.

A total of nineteen analyses were performed in 19 different zircon crystals, which returned 18 analyses with discordance up to 2%, and only one with discordance of 7%. The dataset exhibits variable Th (51.87 – 391.40 ppm; mean = 144.2 ppm), and U (87.02 – 406.18 ppm; mean = 177.27 ppm) concentrations, besides slightly heterogeneous Th/U ratios (0.47 < Th/U < 1.48; mean = 0.82). Such values are in coherence with the zircon of igneous origin. In addition, low ^{204}Pb values were obtained and, therefore, within the acceptable limits.

Collectively, 18 analyzed spots produced discordance up to 2%, whereas only one exhibits discordance of 7%. The analysis provided a concordant age of 1984.9 ± 5.2 Ma (MSWD = 1.2; n = 19; Figure 10A), considered as the crystallization age regarding the igneous protolith. Based exclusively on analysis with discordance of 0% (n = 06), the data return a $^{206}Pb/^{238}U$ age-weighted mean of 1,987 ± 15 Ma (MSWD = 0.56; Figure 10B). Furthermore, two different zircon crystals cores yielded ages of 2,005 ± 22 Ma and 2,000 ± 19 Ma, whereas their respective rims returned ages of 1,963 ± 20 Ma and 1,966 ± 19 Ma.

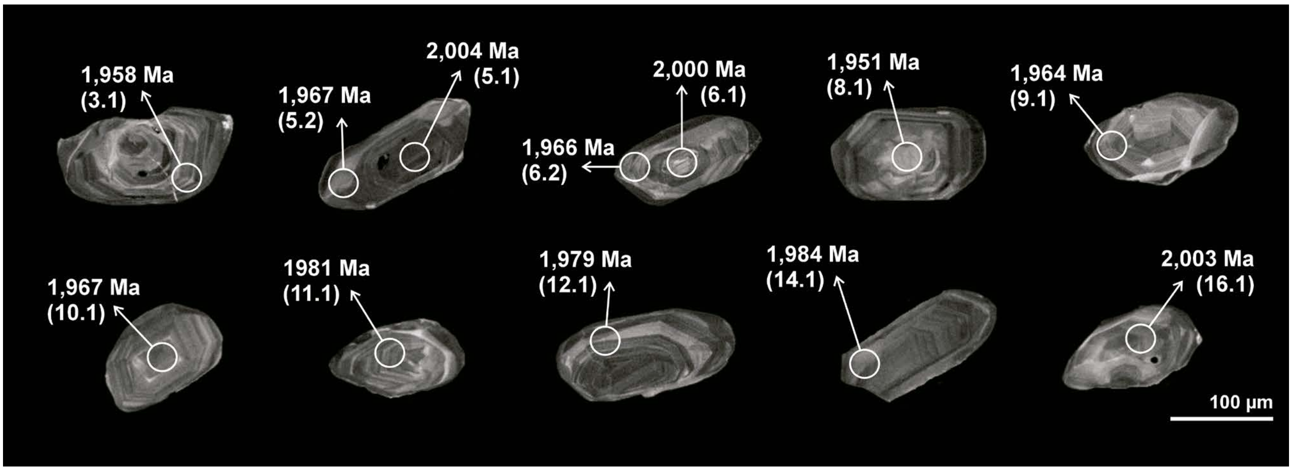

Figure 9. Cathodoluminescence images of zircon crystals from orthogneiss mylonite (AGRB-15 sample), with individual $^{207}Pb/^{206}Pb$ ages spot locations.

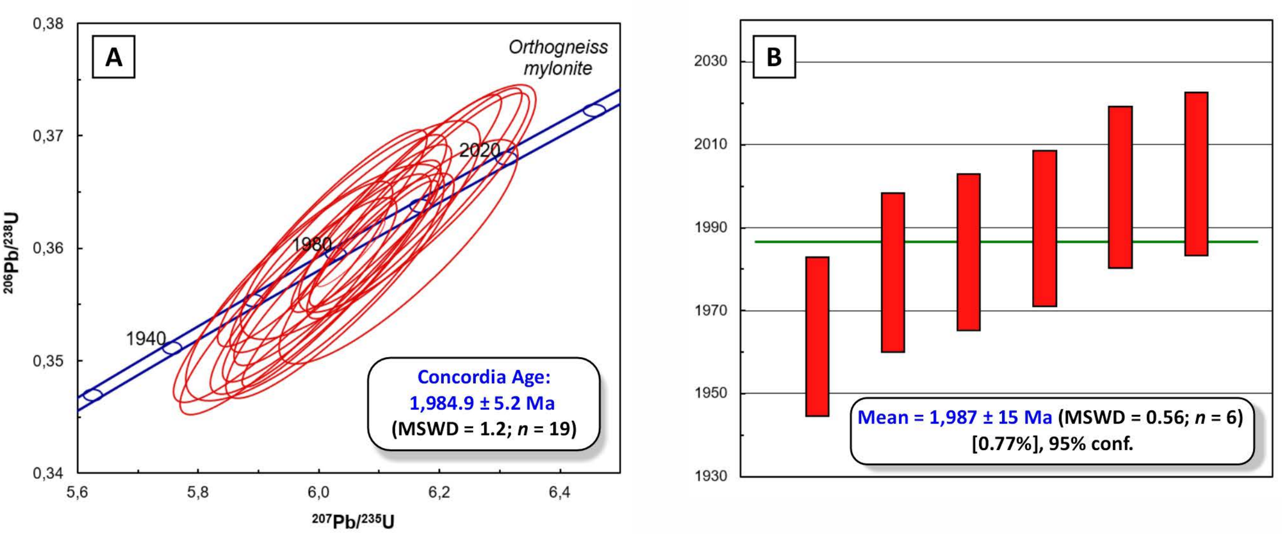

Figure 10. (A) Zircon U–Pb concordia age diagram yielding an age of 1,984.9 ± 5.2 Ma; and (B) $^{207}Pb/^{206}Pb$ weighted aos verage age plot resulting an age of 1,987 ± 15 Ma, both calculated from zircon crystals analysis extracted from orthogneiss mylonite (AGRB-15 sample; discordance of ca. 0%).

DISCUSSION

Hydrothermal system evolution

The albite-rich alteration (sodic-like alteration) corresponded to the initial stage concerning the hydrothermal activity that took place at the Aguinaldo gold occurrence. This alteration is characterized by the enrichment of Na-Si in opposition to depletion in Ca and K, due to albite formation over igneous feldspars (Engvik et al., 2008; Hövelmann et al., 2010). The presence of Na-enriched fluids could be attributed both to high temperatures (600° < T < 450° C; Dilles and Einaudi, 1992) and to neutral to faintly alkaline fluids (Seedorff et al., 2005).

The potassic alteration allowed the K-Feldspar formation over the previous hydrothermal stage. Similar temperatures (400° < T < 550 °C) and pH (neutral to alkaline) are usually attributed to K-Feldspar formation from calc-alkaline-derived exsolved fluids, especially those from granodiorite to quartz monzonitic composition (Pirajno, 1992; Sillitoe, 2010). Such attribution is coherent with the granodioritic composition of the host rock of the Aguinaldo gold occurrence. The replacement of igneous and metamorphic orthoclase by hydrothermal albite may have promoted the K^+ release to fluids, therefore, increasing the aK^+, essential to K-Feldspar formation during the potassic alteration. Moreover, the formation of hematite reflects oxidizing fluids conditions, therefore, promoting the pH lowering by sulfate reduction, which releases S^{2-} to fluid. These conditions may have favored the chalcopyrite and pyrite precipitation (Faure, 1986; Seedorff et al., 2005; Sun et al., 2015).

The sericite-muscovite alteration overprints the preexisting alterations, due to the feldspars hydrolysis from acidic fluid conditions driven by high aH^+ (Guilbert and Park, 1986). The EMPA analysis returned Al-rich and Al--Fe-rich muscovite and sericite, possibly resulting from acidy fluids during temperature decreasing (ca. 200 – 250°C), consequently, causing the leaching of Ca^{2+}, Na^+, and Ca^+ from igneous feldspars (Barnes, 1997; Robb, 2005; Sun et al., 2015).

Posteriorly, the hydrothermal system evolved to the silica injections stage, simultaneously to gold precipitation. According to Rimstidt (1997), the silica solubility is inversely proportional to temperature and pressure increase. Moreover, the usual presence of comb-quartz veins further evidence fluid circulation at shallow crustal levels at low to moderate temperatures (ca. 200 – 300°C) (Barnes, 1997; Candela, 1997; Seedorff et al., 2005). This temperature range may have been influenced by colder, oxidizing external fluids (meteoric fluids?).

The formation of pervasive and veinlet-type calcite, in magmatic-hydrothermal-dominated processes, could indicate low-salinity, neutral to alkaline, and water-heated CO_2-rich fluids, therefore, under high partial pressure of carbon dioxide (P_{CO_2}) (Simmons and Browne, 2000; Robb, 2005; Simpson et al., 2004). The condensation and absorption of CO_2 loss during boiling processes are usually related to the genesis of such fluids (Hedenquist and Henley, 1985; Simpson et al., 2004). If the system were close to calcite saturation conditions, its formation would be facilitated by minimal heating of CO_2-rich fluids, as the consequence of its retrograde solubility, as reported in epithermal systems (Simmons and Christenson 1994; Brathwaite et al., 2000; Simpson et al., 2004).

Moreover, several studies have discussed that carbonate solubility is inversely proportional to temperature increases, but directly proportional to pressure increment (Ellis, 1963; Barnes, 1997; Newton and Manning, 2002; Duan and Li, 2008). Furthermore, in low-temperature aqueous fluids (below 300° C), the CO_2 exhibits low solubility (Rimstidt, 1997). Within this temperature range, carbonic acid (H_2CO_3) corresponds to the dominant CO_2^{3-}component, whose dissociation is enhanced by a slight reduction in pH, which promotes the leaching of cations and, consequently, the generation of bicarbonate-rich fluids (Bischoff and Rosenbauer, 1996). Nevertheless, that situation may not have taken place at Aguinaldo, since the brunsvigite and ripodolite temperatures formation, achieved by chlorite geothermometer, were close to or above 300° C.

Hence, the extensive pervasive carbonate alteration identified at Aguinaldo may be linked to CO_2 loss by boiling processes rather than the dissociation of carbonic acid. Additional evidence for CO_2-enriched fluids corresponds to the presence of three-phase saline fluid inclusions (aqueous, vapor bubble, and the daughter solid phases) related to mineralizing fluids, as reported by Cenatti (2019).

Dehydration and devolatilization processes triggered by metamorphism could also contribute to H_2O-CO_2-rich-forming fluids at Aguinaldo. However, the $\delta^{13}C$ and $\delta^{18}O$ values from calcite concentrates extracted from carbonate alteration, and the $\delta^{34}S$ from pyrite derived from ore, returned a strong magmatic signature for carbon, oxygen, and sulfur (Mariano, 2021; Pilon and Pereira, 2023), not corroborating, therefor, to metamorphic-hydrothermal sources. Although aqueous-carbonic fluids are dominantly responsible for transporting and precipitating gold in most mesothermal gold deposits, saline fluids, analogous to the preceding case, are significantly incompatible with this ore-forming process (Groves et al., 1998; Wyman et al., 2016; Gaboury, 2019).

The laterally zoned veins sequence outwards toward widely expressive and dominant chlorite alteration. This stage may have resulted from progressive dilution and neutralization of the previous faintly acidic condition through high wall-rock interaction and possibly the mixing with oxidizing and colder external fluids (meteoric?). The clinochlore and chamosite formation are indicative of Fe-Mg-rich solutions. During it, the temperature may have lowered to ca. 200 – 300°C, with the increase in aK^+/aH^+ ratios (Robb, 2005), supported by the chlorite geothermometer (from 242 to 420° C). According to Barnes (1997), the replacement of igneous minerals (e.g. plagioclase, magnetite, and biotite) during the sericite-muscovite alteration may have promoted the increase of Fe, Mg, Ca, Ti, and P concentrations in the fluids, as observed at Aguinaldo occurrence. The mineral paragenesis represented by Fe-Mg-chlorite, titanite, rutile, monazite, apatite, and low-crystallinity hematite restricted to chlorite edges, represent petrographic issues concerned to such fluid enrichment. The lowering of fluid temperature could have favored the iron release from the chlorite structure, with hematite formation in its edges and cleavage planes (Deer et al., 2000).

The late-stage hydrothermal evolution of the Aguinaldo occurrence is represented by silica-infill, responsible for generating barren quartz veinlets that crosscut the previous hydrothermal alterations. This stage may be associated to the ceasing of hydrothermal circulation, possibly due to the mixing with external fluids (meteoric), under low-temperature conditions.

Collectively, the identification of low-temperature hydrothermal alteration patterns (e.g. silicification, silica infill, sericite, and carbonate alterations) over deeper alteration types (e.g. albite and potassic alterations) may represent the thermal collapse of the hydrothermal cell in response to strong hydrolytic alteration due to mixing of magmatic fluids with meteoric fluids (Seedorff et al., 2005; Sillitoe, 2010), resulting in the telescoping-building process.

Ore-forming mechanisms

The Aguinaldo structurally-controlled gold mine exhibits ore paragenesis mainly composed of pyrite and chalcopyrite that host sphalerite, galena, gold, and minor silver inclusions. According to the log fO_2-pH diagram (Figure 11), the coexistence of pyrite and chalcopyrite states moderates redox conditions, however, a wide pH range: from very acidic to faintly alkaline conditions. If considered that hydrothermal quartz and carbonate stabilities require pH under neutral to alkaline conditions, together with the inversely proportional zinc and lead solubility to pH increasing (Li et al., 2022), it is possible to restrict the pH and redox ranges responsible for quartz + sulfide ± carbonate veins forming processes. It is assumed, therefore, that moderate redox and neutral to slightly alkaline pH conditions were performed during ore-forming processes at the Aguinaldo gold occurrence. In this context, the mineralizing fluid has experienced pH-increasing processes as those responsible for lowering the gold solubility in the mineralizing fluid (Figure 11).

Based on the existence of comb-texture quartz veins, the low to moderate chlorite temperatures formation, the possible deformed open-spaced filling textures, and the parallel quartz ± carbonate veins, the Aguinaldo occurrence may have formed by hydrothermal fluid circulation under shallow crustal level and low-medium temperatures fluids. In these conditions, gold and silver are more efficiently transported as hydrosulfide complexes (e.g. AuHS, $Au(HS)_2^-$), such as observed in most epithermal environments (Seward, 1973; Shenberger and Barnes, 1989; Hayashi and Ohmoto, 1991; Benning and Seward, 1996; Stefánsson and Seward, 2003, 2004; Liu et al., 2011; Pokrovski and Dubrovinsky, 2011).

At the Aguinaldo, the high fluid pressure may have caused rock fracture, favoring the fluid circulation, intensive pervasive hydrothermal alteration patterns, and the formation of quartz + sulfide ± carbonate veins by mineralizing fluids. These processes may have favored the intense silica injection and the metals precipitation by lowering the temperature and increasing pH conditions (Figure 11). Collectively, it may have been triggered by

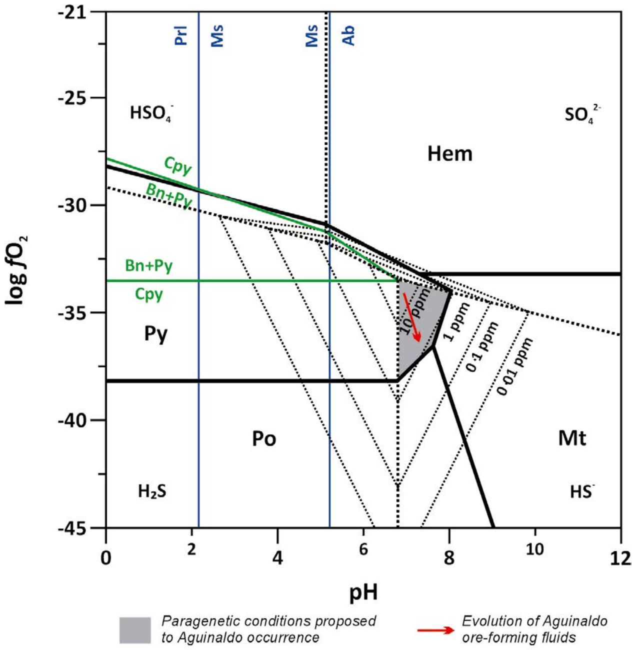

Figure 11. Log fO_2 vs pH diagram exhibiting the physicochemical conditions attributed to mineralizing fluids responsible for transporting and precipitating the gold at the Aguinaldo occurrence.

boiling processes, as often assigned to epithermal and porphyry systems (Seedorff et al., 2005; Heinrich et al., 2004; Sillitoe, 2010).

Moreover, the brunsvigite and minor ripidolite formation in the pervasive chlorite alteration halo demonstrates iron-rich fluids and their intense interaction with host rock. During the hydrothermal chlorite-forming stage, it might has occurred the input of Fe^{2+} into the system. Such iron excess may have favored the restricted disseminated pyrite-forming processes, possibly between 250 to 350° C (Phillips, 1986; Heinrich et al., 2004). John et al. (2010) and Mao et al. (2011) suggest that the slightly neutral fluids derived from chlorite alteration can play as an important proxy for metal precipitation. The chlorite geothermometer here estimated (242° < T < 420° C) corroborates to this interpretation.

At the galleries of Aguinaldo occurrence is observed the infiltration of elevated volume of water from Peixoto river, through faults and fractures systems. The final stage, therefore, is represented by the major input of meteoric fluid to the system, after the hydrothermal fluids circulation has ceased. The ingress of low-temperature oxidizing fluids (meteoric fluids) favored the oxidation reactions of sulfides, resulting in the secondary mineral assemblage formation, the leaching of metallic cations (e.g. Fe^{2+}, Cu^{+}, S^{2+}), and the production of $H_2SO_{4(aq)}$ (acid mine drainage). Digenite and covellite (Cu-sulfides), resulting from chalcopyrite and pyrite oxidation, besides hematite and goethite from pyrite oxidation and hydrolysis reactions, represent the diagnosing secondary mineral assemblage.

Genetic model

The genetic model concerned with structurally-controlled gold occurrences and deposits at the Alta Floresta Gold Province has been controversial, especially if considered their ambiguous descriptive geological attributes (Assis et al., 2014; Juliani et al., 2021; Mesquita et al., 2022). Such proposals have interpreted them as: (i) mesothermal gold deposits (Paes de Barros, 1994; Siqueira, 1997; Madruci, 2000; Santos et al., 2001; Silva and Abram, 2008; Poggi, 2019; Mesquita et al., 2022; Poggi et al., 2022); (ii) intrusion-related gold systems, IGRS (Santos et al., 2001; Abreu, 2004; Bizotto, 2004; Paes de Barros, 2007), and (iii) porphyry-epithermal systems (Moura, 1998; Moura et al., 2006; Assis, 2011, 2015; Rodrigues, 2012; Assis et al., 2014; Trevisan, 2015; Juliani et al., 2021; Trevisan et al., 2021).

At Aguinaldo gold occurrence, the host rock comprises the 1.98 Ga orthogneiss, with apatite, allanite, and magnetite as accessory mineral phases, suggesting it has been derived from calc-alkaline and oxidized-derived magmas. Such geochemical and geochronological signatures are compatible with rocks belonging to Cuiú-Cuiú Complex, which share affinity with calc-alkaline, oxidized and metaluminous granitoids (I-type granites) (Klein et al., 2001).

The ore zones show a polymetallic signature (Au, Ag, Cu, Zn and Pb), composed of major pyrite, chalcopyrite, and gold, with minor silver, sphalerite, and galena. The abundance of chalcopyrite, together with the base metal signature, are dissonant to mesothermal gold deposit, due to the absence of Cu-rich sulfide phases in their mineral paragenesis (Goldfarb et al., 2001, 2005; Goldfarb and Groves, 2015; Zhong et al., 2015; Gaboury, 2019). It is known that copper is efficiently transported by saline mineralizing fluids, such as described in Mississippi-valley type (MVT; Leach et al., 2005, 2010; Paradis et al., 2007; Anderson, 2008), sedimentary exhalative (SEDEX; Leach et al., 2005; Goodfellow and Lydon, 2007; Cooke et al., 2000), porphyry and base metals epithermal deposits (Tosdal et al., 2009; Sillitoe, 2010; Sun et al., 2015, 2017; Hurtig et al., 2021). Metamorphic-derived solutions, however, are known by their low-salinity fluid signature (Goldfarb et al., 2005; Zhong et al., 2015; Gaboury, 2019).

Moreover, the physicochemical conditions required for magmatic-sourced fluids transport and precipitate copper, zinc, and lead are found in intermediate-sulfidation epithermal systems (Tosdal et al., 2009; Hurtig et al., 2021). Magma-derived base metals-rich fluids can efficiently transport metals at low to moderate temperatures (ca. 260° < T < 400° C) and from intermediate to very-low fS_2 conditions (Einaudi et al., 2005). Although the Aguinaldo gold occurrence exhibits galena and sphalerite as small inclusions in Cu-Fe-sulfides, is notable the coexistence between pyrite and chalcopyrite. This petrographic evidence is coherent with ore-forming processes linked to intermediate-sulfidation epithermal deposits (Figure 12).

Based on mineralized quartz + sulfide veins, the hydrothermal alteration is zoned. The paragenetic temporal evolution concerning the distal and deeper hydrothermal alterations comprises (1) an incipient pervasive albite-rich alteration, obliterated by (2) an intensely developed potassic alteration with pervasive reddish K-Feldspar. These stages are temporally followed by colder, proximal, and shallower hydrothermal alterations paragenesis represented by (3) pervasive sericite-muscovite alteration; (4) silicification and silica infills that favored quartz-veins formation; (5) intensive pervasive carbonate alteration; (6) wide chlorite-rich alteration; and finally, (7) late silica infills with generation of later quartz-veinlets. It is observed that the moderate-low temperatures paragenesis have obliterated those of higher temperatures, suggesting an effective telescoping process at Aguinaldo gold mineralization.

Overall, the Aguinaldo gold occurrence is characterized by (i) structurally-controlled mineralization in quartz + sulfide ± carbonate veins; (ii) ortho-derived photolith host rock; (iii) ore paragenesis composed of precious and base metals, suggesting low to intermediate sulfur activity (e.g. pyrite, chalcopyrite, sphalerite, and galena); (iv) presence of comb quartz veins; (v) gold with high silver contents; and (vi) according to Cenatti (2019), aqueous biphasic fluid inclusions in coexistence with restricted aqueous-carbonic and three-phase saline inclusions. These attributes advocate moderate $ƒO_2$, intermediate to very-low $ƒS_2$ conditions, in conjunction with moderate temperatures (Figure 12), suggesting fluid percolation at shallow crustal level, possibly derived from boiling processes triggered under decompression of magmatic-hydrothermal fluids. Although the chlorite geothermometer data (200º < T < 400º C) are not fully compatible with intermediate-sulfidation systems, since their fluid temperatures are usually lower than 300° C, such values do not exclude that conclusion. Overall, the Aguinaldo mineralization exhibits characteristics comparable to other gold occurrences from AFGP.

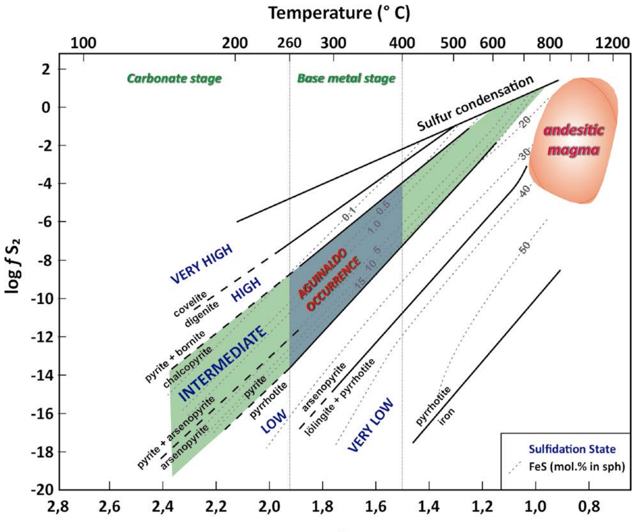

Figure 12. Log ƒS2 vs temperature diagram (Extracted from Einaudi et al., 2005), exhibiting the relative sulfidation state regarding epithermal systems classification plotted over a grid of mineral sulfidation reactions. The positioning of the structurally-controled Aguinaldo gold occurrence, here classified as similar to intermediate-sulfidation epithermal deposits, was suggested based on the mineral paragenesis identified within its ore zone.

On the other hand, few important characteristics observed in epithermal deposits were not identified at Aguinaldo occurrence, such as: (i) ore-hosting felsic volcanic rocks; (ii) lölingite, tennantite, sphalerite, and galena as major sulfide phases; (iii) adularia and/or barite as important gangue hydrothermal minerals; and (iv) illite-rich or smectite-rich argillic alterations.

Hence, the ore precipitation in the Aguinaldo occurrence could have been linked to ore-forming processes similar to those described in intermediate-sulfidation epithermal systems (Figure 12) (Corbett and Leach, 1997; Hedenquist et al., 2000; Simmons et al., 2005; Taylor, 2007), however, pre- or sin-deformation. Such a conclusion opens an important issue concerning the gold and base metals fertility of Paleoproterozoic provinces in housing porphyry and epithermal deposits, which are usually focused on Cenozoic Provinces mainly composed of calc-alkaline arc-derived magmas (Hedenquist et al., 2000; Seedorff et al., 2005; Taylor, 2007; Sillitoe, 2010), as exemplified by Andes, Indonesia, and Philippines.

Therefore, the Paleoproterozoic calc-alkaline magmatic events that took place at AFGP played a significant role in building the ore-forming processes responsible for its porphyry and epithermal-like gold occurrences.

CONCLUSION

The present investigation points out that Aguinaldo gold occurrence is similar to intermediate-sulfidation gold deposits. Such conclusion is concerned with the major following descriptive and geochemical data:

1. Aguinaldo occurrence is hosted by 1.98 Ga felsic orthogneiss mylonite, correlated to 2.0 – 1.97 Ga Cuiú-Cuiú Complex.
2. The sulfide-rich zones occur as barren disseminated pyrite ± chalcopyrite ± hematite ± magnetite ± apatite within the chlorite alteration that envelopes the structurally-controlled ore zone, defined by quartz + sulfide ± carbonate veins.
3. The sulfide-rich zones exhibit a polymetallic signature composed of chalcopyrite + pyrite + gold ± silver ± sphalerite ± galena ± bismuthinite.
4. The hydrothermal alteration temporal evolution is defined as poorly developed pervasive albite alteration, pervasive K-Feldspar alteration telescoped by pervasive sericite-muscovite alteration, silicification, and quartz-rich veins formation, intensive pervasive carbonate alteration, overprinted by pervasive chlorite alteration, and late quartz veins and veinlets.

5. The EMPA analyses performed in chlorite returned brunsvigite and minor ripidolite compositions, formed in the range from 242 to 420° C.
6. Based on EMPA analyses, the white mica is of muscovite composition.
7. Comb-texture quartz veins suggest fluid circulation in shallow crustal level environment (<2km depth).
8. Decreases in temperature and redox conditions, together with the increase of pH may have been important issues for transporting and precipitating the gold by ore-mineralizing fluids, possibly triggered by boiling process.
9. The previous features suggest that the Paleoproterozoic calc-alkaline magmatism may have been responsible for the gold ore-forming processes that took place at AFGP.

ACKNOWLEDGMENTS

The authors thank to Fundação Coordenação de Aperfeiçoamento de Pessoal de Nível Superior (CAPES) for master's scholarship assistance. To Companhia Matogrossense de Mineração (METAMAT) and Cooperativa dos Garimpeiros do Vale do Rio Peixoto (COOGAVEPE) for supporting the activities during the fieldtrip, besides for allowing the acess to Aguinaldo gold occurrence. Moreover, special thanks to Conselho Nacional de Desenvolvimento Científico e Tecnológico (CNPq) for funding the Research Group Project (Process n° 422758/2021-3).

REFERENCES

Abreu, M. C. (2004). *Alteração hidrotermal e mineralização aurífera do depósito de Novo Mundo, região de Teles Pires-Peixoto de Azevedo, Província de Alta Floresta (MT)*. Trabalho de Conclusão de Curso. Campinas: Instituto de Geociências, UNICAMP, 29p.

Almeida, F. F. M. (1978). *Tectonic map of South América, 1:5.000.000 - Explanatory note*. Brasília: DNPM, 23 p.

Alves, C. L., Rizzotto, G. J., Rios, F. S., Barros, M. A. D. S. A. (2020). The Orosirian Cuiú-Cuiú magmatic arc in Peixoto de Azevedo domain, Southern of Amazonian craton. *Journal of South American Earth Sciences*, 102, 102648. https://doi.org/10.1016/j.jsames.2020.102648

Alves, C. L., Rizzotto, G. J., Rios, F. S., Gonçalves, G. F. (2019). *Evolução crustal e metalogenia da Província Mineral Juruena-Teles Pires: estado de Mato Grosso.* Relatório Integrado. Brasília: Serviço Geológico do Brasil, SGB-CPRM. 231p. Available at: https://rigeo.sgb.gov.br/handle/doc/21324. Accessed on: Aug 31, 2023.

Amaral, G. (1974). *Geologia Pré-Cambriana da região amazônica*. Tese (Livre Docência). São Paulo: Instituto de Geociências, USP, 212p. https://doi.org/10.11606/T.44.2016.tde-24062016-160651

Anderson, G. M. (2008). The mixing hypothesis and the origin of Mississipi Valley-type ore deposits. *Economic Geology*, 103(8), 1683-1690. https://doi.org/10.2113/gsecongeo.103.8.1683

Anderson, J. L. (1996). Status of thermobarometry in granitic batholiths. *Earth and Environmental Science Transactions of the Royal Society of Edinburgh*, 87(1-2), 125-138. https://doi.org/10.1017/S0263593300006544

Assis, R. R. (2011). *Depósitos auríferos associados ao magmatismo granítico do setor leste da Província de Alta Floresta (MT), Cráton Amazônico: tipologia das mineralizações, modelos genéticos e implicações prospectivas.* Dissertação (Mestrado). Campinas: Instituto de Geociências – UNICAMP. https://doi.org/10.47749/T/UNICAMP.2011.808405

Assis, R. R. (2015). *Depósitos auríferos associados ao magmatismo félsico da Província de Alta Floresta (MT), Cráton Amazônico: litogeoquímica, idade das mineralizações e fonte dos fluidos.* Tese (Doutorado). Campinas: Instituto de Geociências – UNICAMP. https://doi.org/10.47749/T/UNICAMP.2015.950733

Assis, R. R., Xavier, R. P., Creaser, R. A. (2017). Linking the Timing of Disseminated Granite-Hosted Gold-Rich Deposits to Paleoproterozoic Felsic Magmatism at Alta Floresta Gold Province, Amazon Craton, Brazil: Insights from Pyrite and Molybdenite Re-Os Geochronology. *Economic Geology*, 112(8), 1937-1957. https://doi.org/10.5382/econgeo.2017.4535

Assis, R. R., Xavier, R. P., Paes de Barros, A. J., Barbuena, D., Trevisan, V. G., Ramos, G. S., Santos, T. J. S. (2014). *Depósitos de Au e metais de base associados a sistemas graníticos paleoproterozóicos do setor leste da Província de Alta Floresta (MT), Cráton Amazônico. Metalogenia das Províncias Tectônicas Brasileiras.* Belo Horizonte: Serviço Geológico do Brasil, SGB-CPRM. 611p. Available at: https://rigeo.sgb.gov.br/handle/doc/19389. Accessed on: Jul 15, 2022.

Barnes, H. L. (1997). *Geochemistry of Hydrothermal Ore Deposits* (6th ed.). New York: John Wiley & Sons.

Barros, M. A. S., Barros, A. J. P., Santos, J. O. S., Rocha, M. L. B. P. (2015). Extension of the Tapajós domains to the Alta Floresta gold province: Evidence from U-Pb SHRIMP ages of the Nhandu intrusive suite at 1962 and 1967 Ma. In: *XIV Simpósio de Geologia da Amazônia*, Anais... 400 (CD-ROM). Belém: SBG.

Benning, L. G., Seward, T. M. (1996). Hydrosulphide complexing of Au (I) in hydrothermal solutions from 150 – 400C and 500 – 1500bar. *Geochimica et Cosmochimica Acta*, 60(11), 1849-1871. https://doi.org/10.1016/0016-7037(96)00061-0

Bettencourt, J. S., Juliani, C., Xavier, R. P., Monteiro, L. V., Neto, A. C. B., Klein, E. L., Pereira, V. P. (2016). Metallogenetic systems associated with granitoid magmatism in the Amazonian Craton: An overview of the present level of understanding and exploration significance. *Journal of South American Earth Sciences*, 68, 22-49. https://doi.org/10.1016/j.jsames.2015.11.014

Bini, E. G., Barros, M. A. S., Pierosan, R., Santos, J. O. S. (2015). Petrography and geochronology of felsic volcanic rocks at the eastern portion of Serra do Cachimbo, south-central Amazonian Craton, Brazil. In: *VI Simpósio de Vulcanismo e Ambientes Associados*, Anais... 67 (CD-ROM). São Paulo: SBG.

Bischoff, J. L., Rosenbauer, R. J. (1996). The alteration of rhyolite in CO_2 charged water at 200 and 350 C: The unreactivity of CO_2 at higher temperature. *Geochimica et Cosmochimica Acta*, 60(20), 3859-3867. https://doi.org/10.1016/0016-7037(96)00208-6

Bizotto, A. C. (2004). *Mineralizações auríferas na região de Teles Pires – Peixoto de Azevedo (Mato Grosso), Província de Alta Floresta: O Depósito de Santa Helena.* Trabalho de Conclusão de Curso (Graduação). Campinas: Instituto de Geociências – UNICAMP.

Black, L. P., Kamo, S. L., Allen, C. M., Davis, D. W., Aleinikoff, J. N., Valley, J. W., Mundil, R., Campbell, I. H., Korsch, R. J., Williams, I. S., Foudoulis, C. (2004). Improved $^{206}Pb/^{238}U$ microprobe geochronology by the monitoring of a trace-element-related matrix effect; SHRIMP, ID-TIMS, ELA-ICP-MS and oxygen isotope documentation for a series of zircon standards. *Chemical Geology* https://doi.org/10.1016/j.chemgeo.2004.01.003

Brathwaite, R. L., Simpson, M. P., Faure, K., Skinner, D. N. B. (2000). Telescoped porphyry Cu-Mo-Au mineralisation, advanced argillic alteration and quartz-sulphide-gold-anhydrite veins in the Thames District, New Zealand. *Mineralium Deposita*, 6, 623-640. https://doi.org/10.1007/s001260100182

Candela, P. A. (1997). A review of shallow, ore-related granites: textures, volatiles, and metals. *Journal of Petrology*, 38(2), 1619-1633. https://doi.org/10.1093/petroj/38.12.1619

Carneiro, C. D. C., Carreiro-Araújo, S. A., Juliani, C., Crósta, A. P., Monteiro, L. V. S., Fernandes, C. M. D. (2014). Arcabouço crustal da região sul do cráton Amazonas: evidências geofísicas e implicações tectônicas. In: *XLVII Congresso Brasileiro de Geologia*, Anais... p. 1816. Salvador: SBG. Available at: http://www.sbgeo.org.br/home/pages/44. Accessed on: Aug 15, 2024.

Cathelineau, M., Nieva, D. (1985). A chlorite solid solution geothermometer the Los Azufres (Mexico) geothermal system. *Contributions to Mineralogy and Petrology,* 91(3), 235-244. https://doi.org/10.1007/BF00413350

Cenatti, B. (2019). *Contexto geológico do garimpo de ouro do Agnaldo: um sistema estruturalmente controlado na Província de Alta Floresta (MT).* Trabalho de Conclusão de Curso (Graduação). São Paulo: Instituto de Geociências – USP.

Cooke, D. R., Bull, S. W., Large, R. R., McGoldrick, P J. (2000). The importance of oxidized brines for the formation of australian Proterozoic stratiform sediment-hosted Pb-Zn (Sedex) Deposits. *Bulletin of the Society of Economic Geology,* 96(1), 1-18. https://doi.org/10.2113/gsecongeo.95.1.1

Corbett, G. J., Leach, T. M. (1997). *Southwest Pacific Rim gold-copper systems: structure, alteration, and mineralization*. Colorado: Society of Economic Geologists. https://doi.org/10.5382/SP.06

Dall'Agnol, R., Teixeira, N. P., Rämö, O. T., Moura, C. A., Macambira, M. J., de Oliveira, D. C. (2005). Petrogenesis of the Paleoproterozoic rapakivi A-type granites of the Archean Carajás metallogenic province, Brazil. *Lithos*, 80(1-4), 101-129. https://doi.org/10.1016/j.lithos.2004.03.058

Dardenne, M. A., Schobbenhaus, C. (2001). O escudo do Brasil Central. In: Dardenne, M. A., Schobbenhaus, C. (Eds), *Metalogênese do Brasil*, 1, 46-105. Brasília: Editora Universidade de Brasília/CPRM.

Deer, W. A., Howie, R. A., Zussman, J. (1992). *An Introduction to The Rock-Forming Minerals* (2nd ed). Hertfordshire: Berforts.

Deer, W. A., Howie, R. A., Zussman J. (2000). *Minerais constituintes das rochas: uma introdução* (2ª ed.). Lisboa: Fundação Calouste Gulbenkian.

Dezula, S. E. M. (2016). *Geoquímica e geocronologia do Granito Aragão – Província Aurífera de Alta Floresta, Cráton Amazônico - MT.* Dissertação (Mestrado). Cuiaba: Instituto de Ciências Exatas e da Terra - UFMT.

Dilles, J. H., Einaudi, M. T. (1992). Wall-rock alteration and hydrothermal flows paths about Ann-Mason porphyry copper deposit, Nevada – a 6 km vertical reconstruction. *Economic Geology*, 87, 1932. https://doi.org/10.2113/gsecongeo.87.8.1963

Duan, Z., Li, D. (2008). Coupled phase and aqueous species equilibrium of the H_2O–CO_2–NaCl–$CaCO_3$ system from 0 to 250 °C, 1 to 1000 bar with NaCl concentrations up to saturation of halite. *Geochimica et Cosmochimica Acta*, 72(20), 5128-5145. https://doi.org/10.1016/j.gca.2008.07.025

Duarte, T. B. (2015). *Geologia, geoquímica e geocronologia do domínio vulcânico do arco magmático Juruena, SW do cráton Amazônico: implicações geotectônicas*. Dissertação (Mestrado). Campinas: Instituto de Geociências – UNICAMP. https://doi.org/10.13140/RG.2.1.1657.3203

Einaudi, M. T., Hedenquist, J. W., Inan, E. E. (2005). Sulfidation state of fluids in active and extinct hydrothermal systems: transitions from porphyry to epithermal environments. In: Simmons, S.F., Graham, I. (eds) *Volcanic, geothermal, and ore-forming fluids: rulers and witnesses of processes within the Earth*. Society of Economic Geologists, v.10. https://doi.org/10.5382/SP.10.15

Ellis, A. J. (1963). The solubility of calcite in sodium chloride solutions at high temperatures. *American Journal of Science*, 261(3), 259-267. https://doi.org/10.2475/ajs.261.3.259

Engvik, A. K., Putnis, A., Fitz Gerald, J. D., Austrheim, H. (2008). Albitisation of granitic rocks: the mechanism of replacement of oligoclase by albite. *The Canadian Mineralogist*, 46(6), 1401-1415. https://doi.org/10.3749/canmin.46.6.1401

Faure, G. (1986). *Principles of isotope geology.* (2nd ed.). New York: Cambridge University Press.

Foster, M. D. (1962). *Interpretation of the composition and a classification of the chlorites.* U.S. Geological Survey Professional Paper, 414A, 1-33. Washington: United States Government Printing Office

Gaboury, D. (2019). Parameters for the formation of orogenic gold deposits. *Applied Earth Science*, 118, 124-133. https://doi.org/10.1080/25726838.2019.1583310

Guilbert, J. M., Park Jr, C. F. (1986). *The geology of ore deposits*. Illinois: Waveland Press.

Goldfarb, R. J., Baker, T., Dubé, B., Groves, D. I., Hart, C. J. (2005). Distribution, character, and genesis of gold deposits in metamorphic terranes. In: J. W. Hedenquist, J. F. H. Thompson, R. J. Goldfarb, J. P. Richards (Eds.), *One Hundredth,* Anniversary Volume, 407-450. Ottawa: Society of Economic Geologists. https://doi.org/10.5382/AV100.14

Goldfarb, R. J., Groves, D. I. (2015). Orogenic gold: Common or evolving fluid and metal sources through time. *Lithos*, 233, 2-26. https://doi.org/10.1016/j.lithos.2015.07.011

Goldfarb, R. J., Groves, D. I., Gardoll, S. (2001). Orogenic gold and geologic time: a global synthesis. *Ore Geology Reviews*, 18(1-2), 1-75. https://doi.org/10.1016/S0169-1368(01)00016-6

Goodfellow, W. D., Lydon, J. W. (2007). Sedimentary exhalative (SEDEX) deposits. In: W. D. Goodfellow (Ed.), *Mineral Deposits of Canada: a synthesis of major deposit-types, district metallogeny, the evolution of geological provinces and exploration methods*, 1, 163-183. Toronto: Geological Association of Canada.

Groves, D. I., Goldfarb, R. J., Gebre-Mariam, M., Hagemann, S. G., Robert, F. (1998). Orogenic gold deposits-proposed classification in the context of their crustal distribution and relationship to other gold deposit types. *Ore Geology Reviews*, 13, 7-27. https://doi.org/10.1016/S0169-1368(97)00012-7

Hayashi, K, Ohmoto, H. (1991). Solubility of gold in NaCl- and H2S bearing aqueous solutions at 250 – 350 °C. *Geochimica Cosmochimica Acta*, 55, 2111-2126. https://doi.org/10.1016/0016-7037(91)90091-I

Hedenquist, J. W., Arribas, A., Gonzalez-Urien, E. (2000). Exploration for epithermal gold deposits. *Reviews in Economic Geology*, 13(2), 45-77. https://doi.org/10.5382/Rev.13.07

Hedenquist, J. W., Henley, R. E. (1985). The importance of CO_2 on the freezing point measurements of fluid inclusions: evidence from active geothermal systems and implications of epithermal ore deposition. *Economic Geology*, 80(1), 1379-1408. https://doi.org/10.2113/gsecongeo.80.5.1379

Heinrich, C. A., Driesner, T., Stefansson, A., Seward, T. M. (2004). Magmatic vapor contraction and the transport of gold from the porphyry environment to epithermal ore deposits. *Geology*, 32(9), 761-764. https://doi.org/10.1130/G20629.1

Hövelmann, J., Putnis, A., Geisler, T., Schmidt, B. C., Golla-Schindler, U. (2010). The replacement of plagioclase feldspars by albite: observations from hydrothermal experiments. *Contributions to Mineralogy and Petrology*, 159, 43-59. https://doi.org/10.1007/s00410-009-0415-4

Hurtig, N. C., Migdisov, A. A., Williams-Jones, A. (2021). Are Vapor-Like Fluids Viable Ore Fluids for Cu-Au-Mo Porphyry Ore Formation? *Economic Geology*, 116(7), 1599-1624. https://doi.org/10.5382/econgeo.4835

John, D. A., Ayuso, R. A., Barton, M. D., Blakely, R. J., Bodnar, R. J., Dilles, J. H., Gray, F., Graybeal, F. T., Mars, J. C., McPhee, D. K., Seal, R. R., Taylor, R. D., Vikre, P. G. (2010). *Porphyry Copper Deposit Model.* Scientific Investigations Report. Series: 2010-5070. Reston: U.S. Geological Survey. https://doi.org/10.3133/sir20105070B

Jowett, E. C. (1991). *Fitting iron and magnesium into the hydrothermal chlorite geothermometer*. SSSRN e-Library, 3863523. University of Waterloo/Earth Sciences https://doi.org/10.2139/ssrn.3863523

Juliani, C., Assis, R. R., Monteiro, L. V. S., Fernandes, C. M. D., Martins, E. Z. S. J., Costa e Costa, R. J. (2021). Gold in Paleoproterozoic (2.1 to 1.77 Ga) Continental Magmatic Arcs at the Tapajós and Juruena Mineral Provinces (Amazonian Craton, Brazil): A New Frontier for the Exploration of Epithermal–Porphyry and Related Deposits. *Minerals*, 11(7), 714. https://doi.org/10.3390/min11070714

Juliani, C., Carneiro, C. C., Carreiro-Araújo, S. A., Fernandes, C. M. D., Monteiro, L. V. S., Crósta, A. P. (2013). Estruturação dos arcos magmáticos paleoproterozoicos na porção sul do Cráton Amazônico: implicações geotectônicas e metalogenéticas. In: *XIII Simpósio de Geologia da Amazônia*, Anais..., 157-160. Belém: SBG.

Juliani, C., Carneiro, C. D. C., Fernandes, C. M. D., Monteiro, L. V. S., Crósta, A. P., Carreiro-Araújo, S. A., Aguja, M. A. (2014). Arcos magmáticos continentais paleoproterozoicos superostos na porção sul do cráton Amazônico. In: *XLVII Congresso Brasileiro de Geologia*, Anais, p. 1756. Salvador: SBG. Available at: http://www.sbgeo.org.br/home/pages/44. Accessed on: Nov 5, 2024.

Juliani, C., Fernandes, C. M. D. (2010). Well-preserved late paleoproterozoic volcanic centers in the São Félix do Xingu region, Amazonian Craton, Brazil. *Journal of Volcanology and Geothermal Research*, 191(3-4), 167-179. https://doi.org/10.1016/j.jvolgeores.2010.01.016

Juliani, C., Rye, R. O., Nunes, C. M., Snee, L. W., Silva, R. H. C., Monteiro, L. V., Neto, A. A. (2005). Paleoproterozoic high-sulfidation mineralization in the Tapajós gold province, Amazonian Craton, Brazil: geology, mineralogy, alunite argon age, and stable-isotope constraints. *Chemical Geology*, 215(1-4), 95-125. https://doi.org/10.1016/j.chemgeo.2004.06.035

Klein, E. L., Dos Santos, R. A., Fuzikawa, K., Angélica, R. S. (2001). Hydrothermal fluid evolution and structural control of the Guarim gold mineralisation, Tapajós Province, Amazonian Craton, Brazil. *Mineralium Deposita*, 36(2), 149-164. https://doi.org/10.1007/s001260050295

Kranidiotis, P., MacLean, W. H. (1987). Systematics of chlorite alteration at the Phelps Dodge massive sulfide deposit, Matagami, Quebec. *Economic geology*, 82(7), 1898-1911. https://doi.org/10.2113/gsecongeo.82.7.1898

Leach, D. L., Sangster, D. F., Kelley, K. D., Large, R. R., Garven, G., Allen, C. R., Gutzmer, J., Walters, S. (2005). Sediment-hosted lead-zinc deposits: a global perspective. In: J. W. Hedenquist, J. F. H. Thompson, R. J. Goldfarb, J. P. Richards (Eds.). *One Hundredth Anniversary Volume*. Ottawa: Society of Economic Geology, 561-607p. https://doi.org/10.5382/AV100.18

Leach, D. L., Taylor, R. D., Fey, D. L., Diehl, Saltus, R. W. (2010). *A deposit model for Mississippi Valley-Type lead-zinc ores. Scientific Investigations Report*. Series: 2010-5070. Reston: U.S. Geological Survey. https://doi.org/10.3133/sir20105070A

Li, H., Wang, Q., Weng, W., Dong, C., Yang, L., Wang, X. (2022). Co-precipitation of gold and base metal sulfides during fluid boiling triggered by fault-valve processes in orogenic gold deposits. *Ore Geology Reviews*, 149, 105090. https://doi.org/10.1016/j.oregeorev.2022.105090

Lima-Jr, M. S. (2017). *Geologia, controle e regime de fluidos dos depósitos auríferos na região da fazenda Figueira Branca, SE da PAAF, Terra Nova do Norte/MT*. Dissertação (Mestrado). Cuiabá: Instituto de Ciências Exatas e da Terra - UFMT. Available at: http://ri.ufmt.br/handle/1/3104. Accessed on: Nov 05, 2024.

Liu, X., Lu, X., Wang, R., Zhou, H., Xu, S. (2011). Speciation of gold in hydrosulphide-rich ore-forming fluids: Insights from first-principles molecular dynamics simulations. *Geochimica et Cosmochimica Acta*, 75(1), 185-194. https://doi.org/10.1016/j.gca.2010.10.008

Ludwig, K. R. (2003). User's manual for Isoplot 3.00, a geochronological toolkit for Microsoft Excel. *Berkeley Geochronology Center*, Special Publication no.4. Components.

Madruci, V. (2000). *Avaliação dos produtos integrados TM-Landsat, Radarsat e Gamaespectrométricos na caracterização tectônica e mapeamento geológico de área mineralizada em ouro na região de Alta Floresta-MT.* Dissertação (Mestrado). São José dos Campos: INPE. Available at: http://urlib.net/sid.inpe.br/deise/2000/11.06.11.14. Accessed on: Nov 05, 2024.

Mao, J., Zhang, J., Pirajno, F., Ishiyama, D., Su, H., Guo, C., Chen, Y. (2011). Porphyry Cu-Au-Mo-epithermal Ag-Pb-Zn-distal hydrothermal Au deposits in the Dexing area, Jiangxi province, East China-a linked ore system. *Ore Geology Reviews*, 43(1), 203-216. https://doi.org/10.1016/j.oregeorev.2011.08.005

Mariano, L. G. M. M. (2021). *Assinatura isotópica de carbono e oxigênio do halo de alteração carbonática da ocorrência aurífera do Aguinaldo, Província de Alta Floresta (MT).* Trabalho de Conclusão de Curso. São Paulo: Universidade de São Paulo, 59p.

Massonne, H. J., Schreyer, W. (1987). Phengite geobarometry based on the limiting assemblage with K-feldspar, phlogopite, and quartz. *Contributions to Mineralogy and Petrology*, 96, 212-224. https://doi.org/10.1007/BF00375235

Mesquita, M. J. M., Gomes, M. E. B., Moreira, I. C., Paes, R. A. S., Martins, H. E. S., Matos, J. H. S. N., Ruggiero, A., Primo, G., Ducart, D. F., Poggi, L., Pimenta, V., Laurentis, L. Z., Kunifoshita, A. M. U. (2022). Paleoproterozoic gold deposits at Alta Floresta Mineral Province, Brazil, two overprinted mineralizing events? In: T. Torvela, J. S. Lambert-Smith, R. J. Chapman (Eds.), *Recent Advances in Understanding Gold Deposits: from Orogeny to Alluvium*, Special Publications, 516, 109-154. London: Geological Society. https://doi.org/10.1144/SP516-2021-64

Miguel-Jr, E. (2011). *Controle Estrutural das mineralizações auríferas e idades U-Pb das rochas encaixantes ao longo do Lineamento Peru-Trairão: Província Aurífera de Alta Floresta, Mato Grosso.* Dissertação (Mestrado). Campinas: Instituto de Geociências – UNICAMP. https://doi.org/10.47749/T/UNICAMP.2011.854358

Moura M.A. (1998). O Maciço Granítico Matupá e o Depósito de Ouro Serrinha (MT): Petrologia, Alteração Hidrotermal e Metalogenia. Tese (Doutorado). Brasília: Instituto de Geociências – UnB. Available at: http://repositorio.unb.br/handle/10482/8040. Accessed on: nov 05, 2024.

Moura, M. A., Botelho, N. F., Olívio, G. R., Kyser, T. K. (2006). Granite-related Paleoproterozoic, Serrinha gold deposit, Southern Amazonia, Brazil: hydrothermal alteration, fluid inclusion and stable isotope constraints on genesis and evolution. *Economic Geology*, 101(3), 585-605. https://doi.org/10.2113/gsecongeo.101.3.585

Newton, R. C., Manning, C. E. (2002). Experimental determination of calcite solubility in H_2O-NaCl solutions at deep crust/upper mantle pressures and temperatures: Implications for metasomatic processes in shear zones. *American Mineralogist*, 87(10), 1401-1409. https://doi.org/10.2138/am-2002-1016

Paes de Barros, A. J. (1994). *Contribuição a geologia e controle das mineralizações auríferas de Peixoto de Azevedo-MT*. Dissertação (Mestrado). São Paulo: Instituto de Geociências – USP. Available at: http://www.teses.usp.br/teses/disponiveis/44/44133/tde-11062015-093350/. Accessed on: Nov 05, 2024.

Paes de Barros, A. J. (2007). *Granitos da região de Peixoto de Azevedo – Novo Mundo e mineralizações auríferas relacionadas – Província Aurífera Alta Floresta (MT)*. Tese (Doutorado). Campinas: Instituto de Geociências – UNICAMP. https://doi.org/10.47749/T/UNICAMP.2007.404585

Paradis, S., Hannigan, P., Dewing, K. (2007). Mississippi Valley-type lead-zinc deposits. In: Goodfellow, W.D. (ed.). *Mineral deposits of Canada: A synthesis of major deposit-types, district metallogeny, the evolution of geological provinces, and exploration methods. Geological Association of Canada*, Special Publication, (5), 185-203. Available at: https://www.researchgate.net/publication/228477629_Mississippi_Valley-type_lead-zinc_deposits_MVT. Accessed on: Nov 05, 2024.

Pessoa, M. R., Andrade, A. F., Nascimento, J. D., Santos, J. O. S., Oliveira, J. R., Lopes, R. C., Prazeres, W. V. (1977). *Projeto Jamanxim: Relatório Final*. Relatório Técnico. Manaus: DNPM/SGB-CPRM.

Phillips, G. N. (1986). Geology and alteration in the Golden Mile, Kalgoorlie. *Economic Geology*, 81(4), 779-808. https://doi.org/10.2113/gsecongeo.81.4.779

Pilon, M. L., Pereira, F. C. (2023). *Assinatura isotópica de enxofre em sulfetos do garimpo aurífero filonar do Aguinaldo, Província de Alta Floresta (MT), Cráton Amazônico.* Relatório Final de Iniciação Científica. São Paulo: Instituto de Geociências – USP.

Pirajno, F. (1992). *Hydrothermal mineral deposits. Principles and fundamental concepts for the exploration geologists*. Berlin: Springer-Verlag.

Poggi, L. (2019). *The Au-Cu-Mo Paraíba deposit (MT): integration of spectral and conventional techniques for mineral exploration.* Dissertação (Mestrado). Campinas: Instituto de Geociências – UNICAMP. https://doi.org/10.47749/T/UNICAMP.2019.1082554

Poggi, L., Ducart, D. F., Mesquita, M. J., Moreira, I. C., Gomes, M. E. B., Souza Filho, C. R. (2022). New Insights into the Evolution and Footprints of the Paraíba Au-Cu-Mo Deposit, Alta Floresta Mineral Province (Brazil), through Integration of Spectral and Conventional Methods. *Minerals*, 12(10), 1327. https://doi.org/10.3390/min12101327

Pokrovski, G. S., Dubrovinsky, L. S. (2011). The S3–ion is stable in geological fluids at elevated temperatures and pressures. *Science*, 331(6020), 1052-1054. https://doi.org/10.1126/science.1199911

Rimstidt, J. D. (1997). Gangue mineral transport and deposition. *Geochemistry of Hydrothermal Ore Deposit*, 3, 487-515. https://doi.org/10.1016/B978-0-08-095975-7.01102-5

Rios, F. S. (2019). *O depósito de Au (Cu-Ag) Serrinha de Guarantã, cráton Amazônico, Brasil: um depósito aurífero não-convencional associado ao sistema pórfiro-epitermal paleoproterozoico Juruena-Teles Pires.* Dissertação (Mestrado). Brasília: Instituto de Geociências – UnB. Available at: http://repositorio.unb.br/handle/10482/36918. Accessed on: Nov 05, 2024.

Rios, F. S., Alves, C. L., Rizzotto, G. J., Gonçalves, G. F. (2018). Implicações na Gênese e controle estrutural das mineralizações auríferas nas rochas do Domínio Peixoto de Azevedo, Província Tapajós-Parima, Cráton Amazônico. In: *XLIX Congresso Brasileiro de Geologia*. Anais... Rio de Janeiro: SBG. Available at: http://www.sbgeo.org.br/home/pages/44. Accessed on: Sep 15, 2024.

Rizzotto, J. G., Alves, C. L., Rios, F. S., Barros, M. A. S. (2019). The Western Amazonia Igneous Belt. *Journal of South American Earth Sciences*, 96, 102326. https://doi.org/10.1016/j.jsames.2019.102326

Robb, L. (2005). *Introduction to ore-forming processes*. Carlton: Blackwel Publishing.

Rocha, M. L. B. P. (2016). *Estudos geoquímicos e geocronológicos aplicados às rochas graníticas do garimpo Trairão-MT.* Dissertação (Mestrado). Brasília: Instituto de Geociências – UnB. Available at: http://repositorio.unb.br/handle/10482/21297. Accessed on: nov 05, 2024.

Rodrigues, R. M. (2012). *Caracterização geológica e metalogenética do Depósito X1 – Província Aurífera de Alta Floresta, Região de Matupá (MT).* Campinas: Instituto de Geociências – UNICAMP.

Santos, J. O. S. (2003). Geotectônica dos escudos das Guianas e Brasil-Central. In: BIZZI, L. A. et al. (Eds). *Geologia, Tectônica e Recursos Minerais do Brasil.* Brasília: SGB-CPRM.

Santos, J. O. S., Groves, D. I., Hartmann, A., Moura, M. A., McNaughton, N. J. (2001). Gold deposits of the Tapajós and Alta Floresta domains, Tapajós-Parima orogenic belt, Amazon Craton, Brazil. *Mineralium Deposita*, 36, 278-299. https://doi.org/10.1007/s001260100172

Santos, J. O. S., Hartmann, L. A., Faria, M. S. G., Riker, S. R., Souza, M. M., Almeida, M. E., McNaughton, N. J. (2006). A compartimentação do Cráton Amazonas em províncias: avanços ocorridos no período 2000-2006. In: *XIII Simpósio de Geologia da Amazônia*, Anais, 9, 156-159. Belém: SBG.

Santos, J. O. S., Hartmann, L. A., Gaudette, H. E., Groves, D. I., McNaughton, N. J., Fletcher, I. R. (2000). A new understanding of the Provinces of the Amazon Craton based on integration of field mapping an U-Pb and Sm-Nd geochronology. *Gondwana Research*, 3(4), 453-488. https://doi.org/10.1016/S1342-937X(05)70755-3

Santos, J. O. S., Van Breemen, O. B., Groves, D. I., Hartmann, L. A., Almeida, M. E., McNaughton, N. J., Fletcher, I. R. (2004). Timing and evolution of multiple Paleoproterozoic magmatic arcs in the Tapajós Domain, Amazon Craton: constraints from SHRIMP and TIMS zircon, baddeleyite and titanite U–Pb geochronology. *Precambrian Research*, 131(1-2), 73-109. https://doi.org/10.1016/j.precamres.2004.01.002

Scandolara, J. E., Correa, R. T., Fuck, R. A., Souza, V. S., Rodrigues, J. B., Ribeiro, P. S. E., Lacerda Filho, J. V. (2017). Paleo-Mesoproterozoic arc-accretion along the southwestern margin of the Amazonian craton: The Juruena accretionary orogen and possible implications for Columbia supercontinent. *Journal of South American Earth Sciences*, (73), 223-247. https://doi.org/10.1016/j.jsames.2016.12.005

Seedorff, E., Dilles, J. H., Proffett, J. M., Einaudi, M. T., Zurcher, L., Stavast, W. J. A., Johnson, D. A., Barton, M. D. (2005). Porphyry deposits: characteristics and origin of hypogene features. In: J. W. Hedenquist, J. F. H. Thompson, R. J. Goldfarb, J. P. Richards (Eds.). *One Hundredth Anniversary* Volume, 251-298. Ottawa: Society of Economic Geology. https://doi.org/10.5382/AV100.10

Shenberger, D. M., Barnes, H. L. (1989). Solubility of gold in aqueous sulfide solutions from 150 to 350 C. *Geochimica et Cosmochimica Acta*, 53(2), 269-278. https://doi.org/10.1016/0016-7037(89)90379-7

Seward, T. M. (1973). Thio complexes of gold and the transport of gold in hydrothermal ore solutions. *Geochimica et Cosmochimica Acta*, 37(3), 379-399. https://doi.org/10.1016/0016-7037(73)90207-X

Siivola, J., Schmid, R. (2007) Recommendations by the IUGS Subcommissionon the Systematics of Metamorphic Rocks: List of mineral abbreviations. Webversion 01.02.07. I*UGS Commission on the Systematics in Petrology*. Available from: https://www.researchgate.net/publication/228629780_Abbreviations_for_Names_of_Rock-Forming_Minerals. Accessed on: Nov 11, 2024.

Sillitoe, R. H. (2010). Porphyry copper systems. *Economic geology*, 105(1), 3-41. https://doi.org/10.2113/gsecongeo.105.1.3

Silva, M. G., Abram, M. B. (2008). *Projeto metalogenia da Província Aurífera Juruena-Teles Pires, Mato Grosso*. Goiânia: SGB-CPRM.

Simmons, S. F., Browne, P. R. L. (2000). Hydrothermal minerals and precious metals in the Broadlands-Ohaaki Geothermal System: implications for understanding low-sulfidation epithermal environments. *Economic Geology*, 95, 971-1000p. https://doi.org/10.2113/gsecongeo.95.5.971.

Simmons, S. F., Christenson, B. W. (1994). Origins of calcite in a boiling geothermal system. *American Journal of Science*, 294, 361-400. https://doi.org/10.2475/ajs.294.3.361

Simpson, M. P., Mauk, J. L., Kendrick, R. G. (2004). Telescoped porphyry-style and epithermal veins and alteration at the central Maratoto valley prospect, Hauraki Goldfield, New Zealand. *New Zealand Journal of Geology and Geophysics*, 47(1), 39-56. https://doi.org/10.1080/00288306.2004.9515036

Siqueira, A. J. B. (1997). *Geologia da mina de ouro Filão do Paraíba, região de Peixoto de Azevedo, norte de Mato Grosso.* Dissertação de Mestrado. Instituto de Geociências, Universidade Federal do Rio de Janeiro, Rio de Janeiro, 98p.

Souza J. P., Frasca A. A. S., Oliveira C. C. (2005). *Geologia e Recursos Minerais da Província Mineral de Alta Floresta. Relatório Integrado*. Brasília: Serviço Geológico do Brasil, SGB-CPRM. 164p. Available at: https://rigeo.sgb.gov.br/handle/doc/10246. Accessed on: Nov 25, 2024.

Stefánsson, A., Seward, T. M. (2003). The stability of chloridogold(I) complexes in aqueous solutions from 300 to 600°C and from 500 to 1800 bar. *Geochimica et Cosmochimica Acta*, 67, 4559-4576. https://doi.org/10.1016/S0016-7037(03)00391-0

Stefánsson, A., Seward, T. M. (2004). Gold(I) complexing in aqueous sulphide solutions to 500°C at 500 bar. *Geochimica et Cosmochimica Acta,* 68, 4121-4143. https://doi.org/10.1016/j.gca.2004.04.006

Sun, W., Huang, Rf., Li, H., Hu, Yb., Zhang, Cc., Sun, Sj., Zhang, Lp., Ding, X., Li, Cy., Zartman, R. E., Ling, Mx. (2015). Porphyry deposits and oxidized magmas. Ore Geology Reviews: *Journal for Comprehensive Studies of Ore Genesis and Ore Exploration*, 65, 97-131. https://doi.org/10.1016/j.oregeorev.2014.09.004

Sun, W., Wang, Jt., Zhang, Lp., Zhang, Cc., Li, H., Ling, Mx., Ding, X., Li, Cy., Liang, Hy. (2017). The formation of porphyry copper deposits. *Acta Geochimica*, 36, 9-15. https://doi.org/10.1007/s11631-016-0132-4

Tappert, M. C., Rivard, B., Giles, D., Tappert, R., Mauger, A. (2013). The mineral chemistry, near-infrared, and mid-infrared reflectance spectroscopy of phengite from the Olympic Dam IOCG deposit, South Australia. *Ore Geology Reviews*, 53, 26-38. https://doi.org/10.1016/j.oregeorev.2012.12.006

Tassinari, C. C. G., Macambira, M. J. B. (1999). Geochronological Provinces of the Amazonian Craton. *Episodes*, 22(3), 174-182. http://doi.org/10.18814/epiiugs/1999/v22i3/004

Taylor, B. E. (2007). Epithermal gold deposits. In: Goodfellow, W.D., ed. *Mineral Deposits of Canada: A synthesis of major deposit-types, district metallogeny, the evolution of geological provinces, and exploration methods: Geological Association of Canada, Mineral Deposits Division*, Special Publication, 5, 113-139. Available at: https://kenaonline.com/files/0040/40861/epithermal_gold_synthesis.pdf. Accessed on: Nov 26, 2024.

Tosdal, R. M., Dilles, J. H., Cooke, D. R. (2009). From source to sinks in auriferous magmatic-hydrothermal porphyry and epithermal deposits. Elements, 5, 289-295. https://doi.org/10.2113/gselements.5.5.289

Trevisan, V. G. (2012). *Metalogênese do ouro no granito novo mundo, setor leste da província aurífera de Alta Floresta (MT), cráton amazônico : alteração hidrotermal e petrografia do minério.* Trabalho de Conclusão de Curso, Campinas: Instituto de Geociências – UNICAMP. 97p. Available at: https://hdl.handle.net/20.500.12733/1619391. Accessed on: Nov 25, 2024

Trevisan, V. G. (2015). *Estudo comparativo entre mineralizações filonares de Au ± Cu e Au + metais de base do setor leste da Província de Alta Floresta (MT), Cráton Amazônico.* Dissertação (Mestrado), Campinas: Instituto de Geociências – UNICAMP. https://doi.org/10.47749/T/UNICAMP.2015.955827

Trevisan, V. G., Hagemann, S. G., Loucks, R. R., Xavier, R. P., Motta, J. G., Parra-Avila, L. A., Petersson, A., Gao, J. F., Kemp, A. I. S., Assis, R. R. (2021). Tectonic switches recorded in a Paleoproterozoic accretionary orogen in the Alta Floresta Mineral Province, southern Amazonian Craton. *Precambrian Research*, 364, 1-43. https://doi.org/10.1016/j.precamres.2021.106324

Wyman, D., Cassidy, K. F., Hollings, P. (2016). Orogenic gold and the mineral systems approach: Resolving fact, fiction and fantasy. *Ore Geology Reviews*, 78, 322-335. https://doi.org/10.1016/j.oregeorev.2016.04.006

Zane, A., Weiss, Z. (1998). A procedure for classifying rock-forming chlorites based on microprobe data. *Rendiconti Lincei*, 9(1), 51-56. https://doi.org/10.1007/BF02904455

Zang, W., Fyfe, W. S. (1995). Chloritization of the hydrothermally altered bedrock at the Igarapé Bahia gold deposit, Carajás, Brazil. *Mineralium Deposita*, 30(1), 30-38. https://doi.org/10.1007/BF00208874

Zhong, R., Brugger, J., Tomkins, A. G., Chen, Y., Li., W. (2015). Fate of gold and base metals during metamorphic devolatilization of a pelite. *Geochimica et Cosmochimica Acta*, 171, 338-352. https://doi.org/10.1016/j.gca.2015.09.013